NUCLEAR SCIENCE AND ENGINEERING: 113, 339-366 (1993)

A New Approach and Computational Algorithm for Sensitivity/Uncertainty Analysis for SED and SAD with Application to Beryllium Integral Experiments

Peter M. Song,* Mahmoud Z. Youssef, and Mohamed A. Abdou

University of California-Los Angeles, School of Engineering and Applied Science
6288 Boelter Hall, Los Angeles, California 90024

Received October 28, 1991
Accepted August 27, 1992

Abstract—*A new approach for treating the sensitivity and uncertainty in the secondary energy distribution (SED) and the secondary angular distribution (SAD) has been developed, and the existing two-dimensional sensitivity/uncertainty analysis code, FORSS, was expanded to incorporate the new approach. The calculational algorithm was applied to the $^{9}Be(n,2n)$ cross section to study the effect of the current uncertainties in the SED and SAD of neutrons emitted from this reaction on the prediction accuracy of the tritium production rate from ^{6}Li (T_6) and ^{7}Li (T_7) in an engineering-oriented fusion integral experiment of the U.S. Department of Energy/Japan Atomic Energy Research Institute Collaborative Program on Fusion Neutronics in which beryllium was used as a neutron multiplier. In addition, the analysis was extended to include the uncertainties in the integrated smooth cross sections of beryllium and other materials that constituted the test assembly used in the experiment. This comprehensive two-dimensional cross-section sensitivity/uncertainty analysis aimed at identifying the sources of discrepancies between calculated and measured values for T_6 and T_7. Without considering the uncertainties in the SED and SAD of the $^{9}Be(n,2n)$ cross section, the uncertainties in T_6 are ~2 to 3% in the Li_2O breeding zone, whereas they are ~10% when the uncertainties in the SED and SAD are included. The contribution from the uncertainties in the SAD was small (~1%) compared with the contribution from the uncertainties in the SED. As for T_7, the uncertainties in the Li_2O zone with and without considering the SED and SAD results are 4 to 7 and 2 to 5.5%, respectively. The estimated uncertainties in T_6 and T_7 could partly cover the observed discrepancies between calculations and measurements, although other sources have been identified. Although the approach followed to complete the uncertainty analysis is not standard because of the absence of an existing file that contains the uncertainty information in the SED and SAD of the $^{9}Be(n,2n)$ reaction, the results obtained by introducing approximations to these data clearly demonstrate the importance of accounting for the uncertainties in the SED and SAD when a complete cross-section sensitivity/uncertainty analysis is to be performed.*

I. INTRODUCTION

Beryllium has been suggested for many conceptual blanket designs[1] for fusion reactors, particularly solid breeder blankets, because of its superior neutron multiplication capability through the $^{9}Be(n,2n)$ reaction, whose threshold energy is low. The need has been realized for "clean" benchmark integral experiments of simple geometry utilizing a 14-MeV point source to verify the adequacy of current computational techniques and nuclear data in assessing neutron multiplication in beryllium. In addition, engineering-oriented integral experiments are also needed to verify the design aspects of utilizing beryllium as a multiplier by enhancing the tritium production rate (TPR) throughout the lithium-bearing breeding material.

In most experiments devoted to the verification of the neutron multiplication power in beryllium, the neutrons leaked from the outer surface of beryllium

*Current address: Bettis Atomic Power Laboratory, P.O. Box 79, West Mifflin, Pennsylvania 15122-0079.

spheres (or shells) of various radii (or thicknesses) are absorbed in an outer absorbing medium (or bath) in cases with and without beryllium to verify the apparent (leakage) multiplication factor. This effort began at Lawrence Livermore National Laboratory[2] (LLNL) and was continued by Cloth et al.,[3] Basu et al.,[4] Nargundkar et al.,[5,6] and Wong et al.[7] In these experiments, calculations using ENDF/B-III, -IV, and -V data generally overestimated the apparent neutron multiplication factor by as much as 15 to 25%, depending on the beryllium radius (or thickness), and the larger discrepancies occurred in the large spheres (or shells). Recently, leakage spectrum measurements from beryllium spheres were carried out by Androsenko et al.,[8] Leshchenko et al.,[9] and Ebi et al.,[10] while Smith and King[11] and Chen et al.[12] performed manganese bath and polyethylene absorption measurements, respectively, for neutron multiplication in beryllium spherical shells. Some of these recent experiments have been analyzed[13] with the Young and Stewart[14] evaluation [denoted the Los Alamos National Laboratory (LANL) evaluation in this paper] and the ENDF/B-VI evaluation[15] (the LLNL evaluation here) for beryllium data. The neutron multiplication was perfectly reproduced[11,16] by the LANL evaluation, while it is anticipated that a lower multiplication[13] will be obtained by the new data of ENDF/B-VI developed at LLNL. Furthermore, in the Kernforschungszentrum Karlsruhe experiment,[10] it was shown that for a 17-cm-thick beryllium spherical shell, there is an underestimation (~12%) in the leakage spectrum in the low-energy range (2.45 MeV to 0.1 MeV) and overestimation (~10%) in the energy range up to ~3 MeV with the LANL evaluation. Above 3 MeV, perfect agreement with the measured spectrum is obtained. When ENDF/B-VI data are used, it is argued that[10,13] a large underestimation will be produced in the neutron spectrum around 1 to 2 MeV, which suggests again that the ^{9}Be(n,2n) cross section of ENDF/B-VI (already ~15% lower than that of LANL at high energies) should be increased.

Oyama and Maekawa[17] performed angular leakage spectrum measurements using a 5-cm-thick cylindrical beryllium slab. When the experiment was analyzed with the LANL evaluation for beryllium, the integrated spectrum was underestimated in the 0.1- to 0.5-MeV energy range, overestimated in the 0.5- to 10-MeV energy range, and underestimated in the energy range above 10 MeV. When this experiment was analyzed[13] with the LANL and the LLNL evaluations by the ANTRA2 code,[18,19] it was found that the reproduction of the experimental spectrum was better with the LANL data than with the LLNL data, especially in the 1-MeV energy range, which also suggests increasing the 14-MeV (n,2n) cross section in ENDF/B-VI.

Aside from the clean benchmark experiments mentioned earlier, several engineering-oriented integral experiments were performed within the ongoing U.S. Department of Energy/Japan Atomic Energy Research Institute (DOE/JAERI) Collaboration Program on Fusion Neutronics where the TPRs for ^{6}Li (T_6) and ^{7}Li (T_7) were measured inside a Li_2O zone (~60 long) located behind a 5-cm-thick beryllium layer. This configuration was carried out in an open-geometry case of the phase I experiments[20-22] and in a closed-geometry case of phases IIA and IIB (Refs. 23, 24, and 25). In the U.S. calculations, three evaluations for beryllium were used, namely, ENDF/B-V, LANL, and ENDF/B-VI (LLNL), to analyze some of these experiments.[26] It was shown, however, that the LLNL data give a better prediction for T_6 and other reaction rates than the LANL data. The LANL data give much improved calculated-to-experimental values (C/E) for local T_6, T_7, and other reaction rates as compared with the ENDF/B-V data. Although the total integrated ^{9}Be(n,2n) cross sections in the LANL and ENDF/B-V evaluations are the same, the improvement was due to the more accurate representation of the secondary energy distribution (SED) and the secondary angular distribution (SAD) of neutrons emitted from this reaction.

The importance of the accuracy in determining the SED and SAD of neutrons emitted from reactions such as (n,2n), (n, inelastic), etc., has thus been realized since neutron transport and subsequent interactions with various nuclides of the transport media depend on the incident neutron energy and direction of those secondary neutrons. In this paper, a new methodology is developed and incorporated in the current two-dimensional sensitivity/uncertainty analysis codes to estimate the uncertainty in a particular design parameter (e.g., T_6 and T_7) due to uncertainties in the SED and SAD of the secondary neutrons emitted from the ^{9}Be(n,2n) reaction. It should be pointed out that readily available data on the uncertainties in the SED and SAD of the ^{9}Be(n,2n) reaction are currently nonexistent, and there is an immediate need to process this information from measured experimental data. However, an approximation to these data was introduced by comparing the multigroup form of the ^{9}Be(n,2n) cross section among three available evaluations. In addition, this approach enabled us to separate effects arising from uncertainties in the SAD from those arising from uncertainties in the SED. The approach was applied to investigate discrepancies between calculations and measurements for T_6 and T_7 behind the beryllium layer in the beryllium-sandwiched (BES) experiment of phase IIA of the DOE/JAERI Collaboration Program.[23-25] Furthermore, an extensive sensitivity/uncertainty analysis was also carried out for other partial integrated cross sections of beryllium and other materials (e.g., ^{7}Li, ^{16}O, ^{6}Li, iron) to quantify the importance of their associated uncertainties on T_6 and T_7 predictions relative to the uncertainties arising from the current inaccuracies in the SED and SAD of the ^{9}Be(n,2n) cross section. The analysis was carried out for each of the three evaluations of beryllium data,

namely, the ENDF/B-V, LANL, and LLNL evaluations, with emphasis on the differences among them for the SED and SAD of the ^{9}Be$(n,2n)$ reaction.

In Sec. II, the features of the ^{9}Be$(n,2n)$ cross section among the three evaluations considered are outlined. The experiment is described in Sec. III, where the C/E values for T_6 and T_7 are given with the three valuations. The new approach to treating sensitivities to the SED/SAD is described in Sec. IV. In Sec. V, the calculational procedures followed in the sensitivity/uncertainty analysis are given. The results of this analysis are given in Sec. VI, and the conclusions and remarks are cited in Sec. VII.

II. BERYLLIUM DATA

The ^{9}Be$(n,2n)$ reaction proceeds by transitions through levels in ^{9}Be, ^{8}Be, and ^{4}He. The levels involved are wide and unstable, and the end result of the reaction is always two neutrons and two alpha particles. Perkins was the first to attempt to include details of this transition. His evaluation was used in ENDF/B-III in the form of a single energy-dependent cross section with an angle-integrated secondary neutron spectra.

In ENDF/B-IV and -V, only four of the ^{9}Be excitation levels (1.68, 2.43, 6.76, and 11.28 MeV) have been considered, each having zero width, and the energy-angle correlation between the emitted neutrons is ignored, although the measured $(n,2n)$ neutron emission spectrum of ^{9}Be shows a strong energy-angle correlation.

The concept of pseudolevels is used in which 33 inelastic levels were chosen by Young and Stewart[14] to fit the neutron emission spectrum measurements of Drake et al.[27] This was done by performing numerical fits to Drake et al.'s experimental double-differential neutron emission cross section (DDX) using smooth inter- and extrapolations. This LANL evaluation significantly improved the ENDF/B-IV and -V data, as pointed in Sec. I. The $(n,2n)$ distributions were based on data for a cluster of real levels near $E_x = 2.429$ MeV and 32 excitation energy bins to represent the $(n,2n)$ continuum levels. The excitation energy bins have half-widths of 0.25 MeV. Comparison of the neutron emission spectrum with ENDF/B-IV and -V beryllium cross sections showed that the importance of the low-lying states was overemphasized in ENDF/B-IV and -V. This was the reason for the overprediction of neutron multiplication in the early beryllium experiments[4-7] by as much as 15 to 25%. In the LANL evaluation, a more appropriate correlation was used for the energy-angle distribution of the emitted neutrons from the ^{9}Be$(n,2n)$ reactions that was ignored in ENDF/B-V, although the total smooth cross section in the two evaluations is almost the same.

Recently, Perkins, Plechaty, and Howerton[15] evaluated the DDX using a Monte Carlo technique to model the angle-energy distributions of the many-particle breakup reaction of beryllium. The evaluated data considered the measurements by Drake et al.,[27] Baba et al.,[28] and Takahashi et al.[29] The new evaluated data of beryllium in ENDF/B-VI are based on the Perkins, Plechaty, and Howerton (or LLNL) evaluation. The LLNL evaluation uses a more appropriate representation of the DDX where the correlated angle-energy distributions of the inelastically scattered neutrons are given as tabulated functions, i.e., pointwise in energy and angle in the laboratory system, whereas the LANL evaluation is given in the Legendre approximation in the center-of-mass system. Thus, the LLNL evaluation lends itself readily to rigorous S_n transport calculations in which DDX data are used directly in the segmented angular space without the need for Legendre approximation. In this analysis, however, the updated version of the NJOY89 processing code[30] was used to generate P_L components of the ENDF/B-VI data for beryllium. In this case, the angular dependence of the tabulated DDX data is numerically fitted by a truncated Legendre series expansion using an S_8 Gaussian quadrature procedure for the integration over the whole angular scattering range.

Figure 1 shows the total integrated cross section of the ^{9}Be$(n,2n)$ reaction above 2 MeV processed (in 30 neutron group of MATXS5 group structure[31]) from the ENDF/B-V, LANL, and LLNL evaluations. In the case of the LANL evaluation, two processing systems were used, namely, the AMPX processing system[32] and the NJOY processing system.[30] One can see from Fig. 1 that the ENDF/B-V and LANL data (processed either with the AMPX or the NJOY processing system) are very similar. Also, the ENDF/B-VI data are lower than the ENDF/B-V and LANL data (by ~10 to 15%) at high energies, as pointed out earlier. As for the SED of the ^{9}Be$(n,2n)$ cross section, Figs. 2, 3, and 4 show this distribution for several incident energies (incident energy group in 30-group structure) for the three evaluations, respectively. In these figures, E_{in} and E_{out} represent the incident and emitted energy, respectively. As shown, the SED in the LLNL evaluation does not extend below ~1 keV (according to the notations used in the figures, $E_{out} \sim 10^b = 1$ keV for $b = 3$). In the LANL evaluation, the cross section extends below 1 keV, but the cross section in this energy range is negligible. In the ENDF/B-V evaluation, however, the SED extends down to very low energies.

III. THE EXPERIMENT

The BES experiment of phase IIA of the DOE/JAERI Collaborative Program on Fusion Neutronics[23-25] was considered for this analysis. The rectangular Li_2O test assembly (86.4 × 86.4 × 60.71 cm) was placed at one end of a rectangular enclosure made of Li_2CO_3, and the deuterium-tritium neutron source, generated from the rotating neutron target, was placed

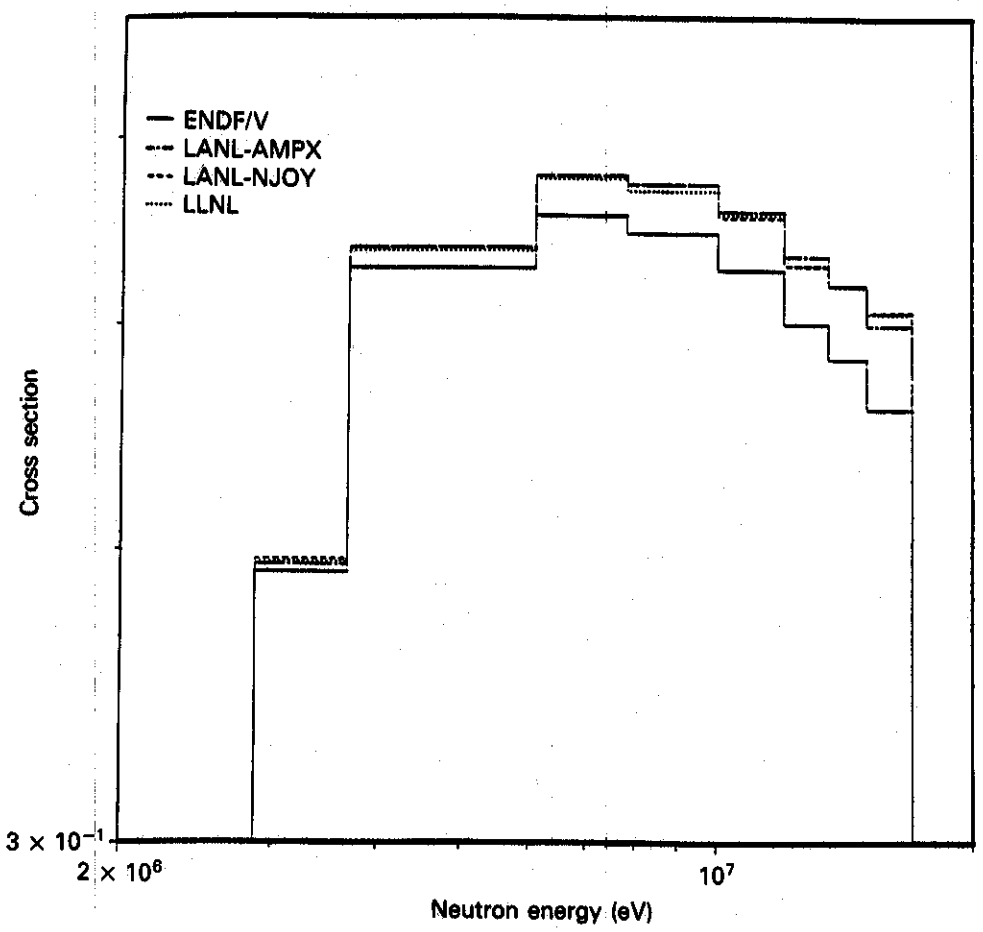

Fig. 1. Processed $^{9}Be(n,2n)$ cross section with various evaluations.

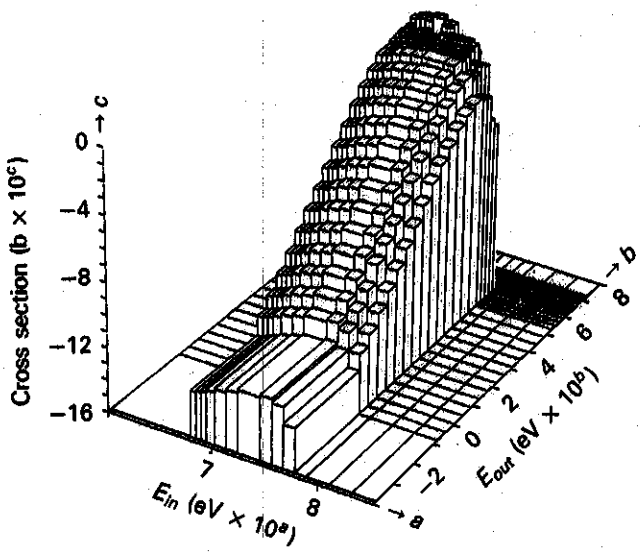

Fig. 2. The SED (cross section) of neutrons emitted from the $^{9}Be(n,2n)$ reaction: ENDF/B-V evaluation.

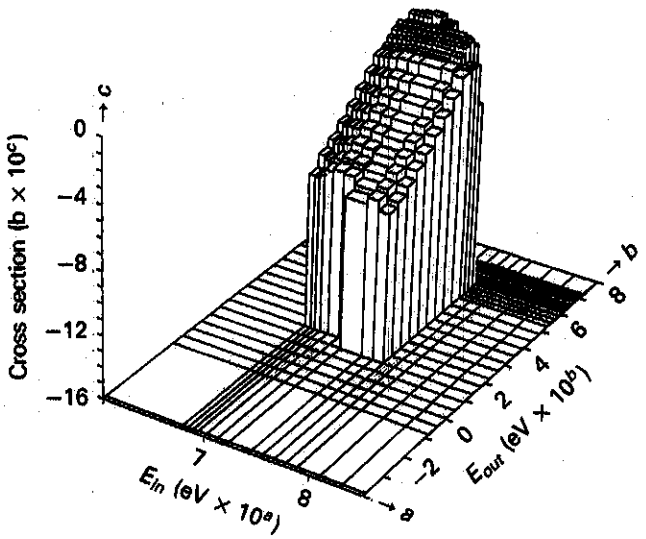

Fig. 3. The SED (cross section) of neutrons emitted from the $^{9}Be(n,2n)$ reaction: LANL evaluation.

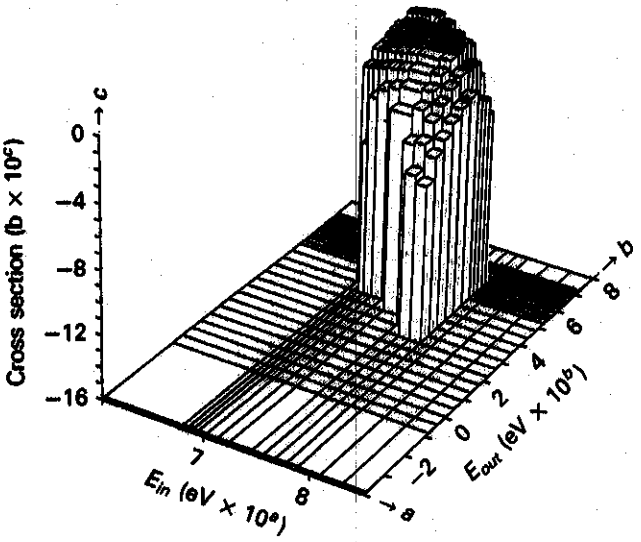

Fig. 4. The SED (cross section) of neutrons emitted from the $^9Be(n,2n)$ reaction: LLNL evaluation.

~78 cm from the square front surface of the test assembly, as shown in Fig. 5. The inner cavity was 87 × 89 × 124 cm, and the thickness of the Li_2CO_3 enclosure was 20.5 cm. A 5-cm-thick polyethylene layer was included at the outer surface of the enclosure to eliminate the low-energy room-returned component of the neutrons reflected by the room walls and reentering the test zone. In this BES experiment, the first 5 cm of the assembly consisted of Li_2O blocks followed by a 5-cm-thick beryllium zone. The rest of the assembly is made of Li_2O blocks following the beryllium layer.

The TPR for ^6Li (T_6) was measured by on-line Li-glass detectors.[33] Other methods (lithium metal and Li_2O pellet) were also used to measure T_6. The TPR from ^7Li (T_7) was measured by the NE-213 indirect method and by lithium metal and Li_2O pellet detectors. Figure 6 shows the C/E values for T_6 and T_7 at several locations throughout the axis of the test assembly. The calculations were performed by the 30-group library of MAXTXS5 (ENDF/B-V) (Ref. 31) and with the three evaluations for beryllium, separately. As shown, the C/E values for T_6 inside the beryllium layer with ENDF/B-V (C/E ~ 1.65) are larger than those obtained by the LANL and LLNL evaluations (~C/E ~ 1.38). This is due to its large $^9Be(n,2n)$ cross section (see Fig. 1), which led to a larger neutron multiplication and hence a larger T_6 in and behind the beryllium layer. Additionally, the SED of the $^9Be(n,2n)$ reaction evaluated by ENDF/B-V exhibits a larger low-energy component, as can be seen from Figs. 2, 3, and 4, with a consequent enhancement in T_6 inside and behind the beryllium layer. In the rest of the Li_2O zone, T_6 is overestimated, particularly with the ENDF/B-V evaluation. The overprediction by the LANL and LLNL evaluations are comparable in the bulk of the assembly (~5 to 8%), but just behind the beryllium layer, there is a sudden drop in the C/E values by as much as 5 to 10% (the largest drop is with the LLNL data).

As for T_7, the ENDF/B-V evaluation gives the largest local values inside the beryllium layer (due to the larger neutron multiplication) but lower values in the bulk of the Li_2O zone as compared with the other evaluations. The T_7 values obtained by the LANL and

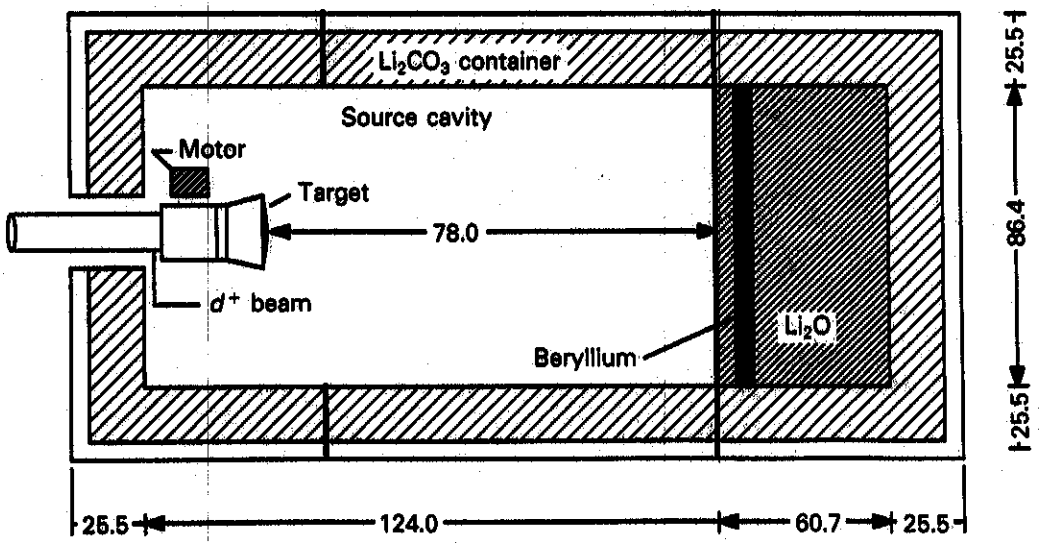

Fig. 5. Geometrical configuration of the BES experiment. Dimensions are given in centimetres.

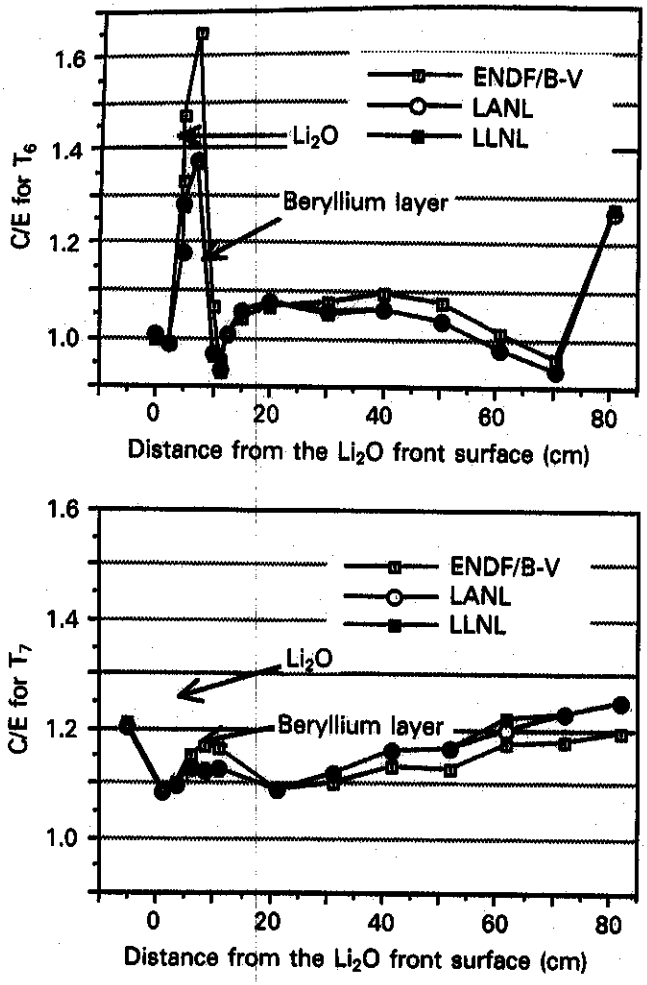

Fig. 6. C/E values for T_6 and T_7 in the BES experiment along the central axis of the test assembly.

LLNL evaluations are comparable (the LLNL values are slightly larger), but generally, T_7 is overpredicted by ~2 to 20% throughout the bulk of the Li_2O zone. The purpose of this analysis is to identify the contribution to the observed discrepancies in T_6 and T_7 that is attributable to the uncertainties in the SED and SAD of the $^9Be(n,2n)$ reaction as well as the uncertainties in the other smooth partial cross sections of beryllium and other materials.

IV. NEW APPROACH FOR TREATING SENSITIVITY TO VARIATIONS IN THE SED AND SAD OF THE $^9Be(n,2n)$ REACTION

IV.A. Previous Approaches

Gerstle et al.[34] and Embrecht[35] introduced the concept of the "hot-cold" SED and the "forward-backward" SAD to analyze the sensitivities to the total SED and SAD. For the hot-cold integral sensitivity, the concept of the median energy $\bar{E}$ of secondary neutrons was introduced in which the probability of emission is equal above and below this energy. This hot-cold integral SED sensitivity expresses the fractional change in the integrated response (e.g., T_6 and T_7) when the number of secondary neutrons that scattered in the hot part of the SED above $\bar{E}$ is increased by 1%, while the number of secondary neutrons scattered into the cold part below $\bar{E}$ is decreased by 1%. Similarly, the forward-backward SAD integral sensitivity can be explained as the fractional change in the integral response when the number of secondary neutrons that were scattered forward is increased by 1%, while the number of secondary neutrons that were scattered backward is decreased by 1% such that the total angle-integrated cross section remains unchanged. Gerstle et al.'s approach is less tedious and simple, but it totally ignores the fact that the measured emission neutron spectrum could be larger (or smaller) than that of the evaluated value over several ranges of the emission energy (or angle) and not over only two ranges as defined by the median energy $\bar{E}$ or the median angle $\bar{\mu}$.

Furuta, Oka, and Kondo[36] followed a more accurate approach to treat the SED by defining standard deviations of the emission spectrum of various reactions in ^6Li and ^7Li over several ranges of the emission spectrum m where direct comparisons between evaluation and measurement were made to derive these standard deviations. They introduced a covariance matrix for integrated areas of SAD and SED, with relative standard deviation (RSD) evaluated by the following formula:

$$\mathrm{RSD}_m = \left| \frac{\left[\int_m P_x(E \to E')\, dE' - \int_m P_e(E \to E')\, dE' \right]}{\int_m P_e(E \to E')\, dE'} \right| . \quad (1)$$

where P_x and P_e are the measured and evaluated SED functions, respectively, and m denotes the m'th integration interval.

IV.B. New Approaches

IV.B.1. Variation in the Secondary Energy Distribution

IV.B.1.a. Variations in the Excitation Levels

Variations in the SED of the emitted neutrons from the $^9Be(n,2n)$ reactions could be achieved in several ways. For example, the beryllium $(n,2n)$ cross section of ENDF/B-V is represented by four excitation levels, each with its own SED. Varying the contribution of a particular level to the total cross section and, at the same time, varying the contribution from other levels such that the total cross section is kept the same will result in a different final SED. In this approach, we have (in multigroup form)

$$\sigma_{gg'} = \sigma_{gg'}^{\chi_1} + \sigma_{gg'}^{\chi_2} + \ldots + \sigma_{gg'}^{\chi_n} = \sum_i^n \sigma_{gg'}^{\chi_i} , \quad (2)$$

where

$\sigma_{gg'} = \sigma_g f(g \to g')$

$f(g \to g')$ = probability distribution function, the probability that neutrons scattered at group g will be transferred to group g'

χ_i = i'th excitation level

n = number of excitation levels involved.

If the cross section of a particular level $\sigma_{gg'}^{\chi_m}$ is changed by a factor α_g^m (the "prime level") and, at the same time, the cross sections of the other levels $\sigma_{gg'}^{\chi_i}$ are varied by factors α_g^i, we get

$$\sigma_{gg'}^{new} = \sum_{\substack{i=1 \\ i \neq m}}^{n} (1 + \alpha_g^i)\sigma_{gg'}^{\chi_i} + (1 + \alpha_g^m)\sigma_{gg'}^{\chi_m} . \quad (3)$$

To keep the total integrated (in energy and angle) cross section the same, we should have

$$\sigma_g^{new} = \sum_{g'} \sigma_{gg'}^{new} = \sigma_g^{old} . \quad (4)$$

By summing Eq. (3) over the exit energy group g', we get

$$\sigma_g^{new} = \sum_{\substack{i=1 \\ i \neq m}}^{n} (1 + \alpha_g^i)\sigma_g^{\chi_i} + (1 + \alpha_g^m)\sigma_g^{\chi_m}$$

$$= \sigma_g^{old} + \sum_{\substack{i=1 \\ i \neq m}}^{n} \alpha_g^i \sigma_g^{\chi_i} + \alpha_g^m \sigma_g^{\chi_m} .$$

Since we force the condition in Eq. (4) to hold in order to keep the total cross section the same at incident energy group g, we get

$$\sum_{\substack{i=1 \\ i \neq m}}^{n} \alpha_g^i \sigma_g^{\chi_i} = -\alpha_g^m \sigma_g^{\chi_m} . \quad (5)$$

There are several ways to vary the cross sections of the excitation levels involved. One method is the "level-independent treatment," in which the variation factors that are applied to each excitation level are assumed to be the same:

$$\alpha_g^1 = \alpha_g^2 = \alpha_g^3 = \ldots = \alpha_g^i = \alpha_g , \quad i \neq m . \quad (6)$$

From Eq. (5), the variation factor that is applied to each excitation level is then given by

$$\alpha_g = -\frac{\alpha_g^m \sigma_g^{\chi_m}}{\sigma_g - \sigma_g^{\chi_m}} . \quad (7)$$

By using the level-independent variation factor α_g, we get a new SED. This can be shown by using Eq. (7) in Eq. (3):

$$\sigma_{gg'}^{new} = \sum_{\substack{i=1 \\ i \neq m}}^{n} (1 + \alpha_g)\sigma_{gg'}^{\chi_i} + \alpha_g^m \sigma_{gg'}^{\chi_m}$$

$$= \sigma_{gg'}^{old} + \sum_{\substack{i=1 \\ i \neq m}}^{n} \alpha_g \sigma_{gg'}^{\chi_i} + \alpha_g^m \sigma_{gg'}^{\chi_m}$$

$$= \sigma_{gg'}^{old} + \frac{-\alpha_g^m \alpha_g^{\chi_m}}{\sigma_g - \sigma_g^{\chi_m}} \sum_{\substack{i=1 \\ i \neq m}}^{n} \sigma_{gg'}^{\chi_i} + \alpha_g^m \sigma_{gg'}^{\chi_m} .$$

By noticing that

$$\sum_{\substack{i=1 \\ i \neq m}}^{n} \sigma_{gg'}^{\chi_i} = \sigma_{gg'}^{old} - \sigma_{gg'}^{\chi_m} ,$$

we get

$$\sigma_{gg'}^{new} = \sigma_{gg'}^{old} - \alpha_g^m \sigma_{gg'}^{\chi_m} \left(\frac{\sigma_{gg'}^{old} - \sigma_{gg'}^{\chi_m}}{\sigma_g - \sigma_g^{\chi_m}} - 1 \right) . \quad (8)$$

Another way of varying the cross section of the excitation levels involved is to assume that the absolute variation in the cross section of other excitation levels is the same:

$$\alpha_g^1 \sigma_g^1 = \alpha_g^2 \sigma_g^2 = \alpha_g^3 \sigma_g^3 = \ldots = \alpha_g^i \sigma_g^{\chi_i} , \quad i \neq m . \quad (9)$$

This method is the "level-dependent treatment." From Eq. (5), the variation factor applied to excitation level χ_i is now given by

$$\alpha_g^i = \frac{-\alpha_g^m \sigma_g^{\chi_m}}{(n-1)\sigma_g^{\chi_i}} , \quad (10)$$

where n is the number of excitation levels that are considered in the treatment. It could be all levels that are energetically possible and contributing to the total cross section, or it could be a selected number of levels. The new SED in this case is given by

$$\sigma_{gg'}^{new} = \sigma_{gg'}^{old} - \frac{\alpha_g^m \sigma_g^{\chi_m}}{(n-1)} \sum_{\substack{i=1 \\ i \neq m}}^{n} \frac{\sigma_{gg'}^{\chi_i}}{\sigma_g^{\chi_i}} + \alpha_g^m \sigma_{gg'}^{\chi_m}$$

$$= \sigma_{gg'}^{old} - \frac{\alpha_g^m \sigma_g^{\chi_m}}{(n-1)} \left[\sum_{\substack{i=1 \\ i \neq m}}^{n} \frac{\sigma_{gg'}^{\chi_i}}{\sigma_g^{\chi_i}} - \frac{(n-1)}{\sigma_g^{\chi_m}} \sigma_{gg'}^{\chi_m} \right] , \quad (11)$$

and the result from the summation over the exit energy group g' shows that the total cross section remains unchanged:

$$\sigma_g^{new} = \sigma_g^{old} - \frac{\alpha_g^m \sigma_g^{\chi_m}}{(n-1)} [(n-1) - (n-1)]$$

$$= \sigma_g^{old} .$$

One important remark about these treatments is that the variation factors α_g^i could be treated as dependent or independent on each excitation level; however, the dependency on the exit energy group g' does not

lead to a new distribution. For example, in the level-independent treatment, if we assume the factors $\alpha_{gg'}$ to be dependent on the exit energy group g', we get

$$\alpha_{gg'}\sigma_{gg'}^{\chi_1} + \alpha_{gg'}\sigma_{gg'}^{\chi_2} \cdots + \alpha_{gg'}\sigma_{gg'}^{\chi_{m-1}} + \alpha_{gg'}\sigma_{gg'}^{\chi_{m+1}} + \cdots = -\alpha_{gg'}^{m}\sigma_{gg'}^{\chi_m} ;$$

i.e.,

$$\alpha_{gg'} = \frac{-\alpha_{gg'}^{m}\sigma_{gg'}^{\chi_m}}{\sigma_{gg'}^{old} - \sigma_{gg'}^{\chi_m}} . \quad (12)$$

The new distribution from these variation factors is exactly the same as the old distribution:

$$\begin{aligned}\sigma_{gg'}^{new} &= \sigma_{gg'}^{old} - \sum_{\substack{i=1\\ i\neq m}}^{n} \frac{\alpha_{gg'}^{m}\sigma_{gg'}^{\chi_m}}{\sigma_{gg'}^{old} - \sigma_{gg'}^{\chi_m}} \sigma_{gg'}^{\chi_i} + \alpha_{gg'}^{m}\sigma_{gg'}^{\chi_m} \\ &= \sigma_{gg'}^{old} - \frac{\alpha_{gg'}^{m}\sigma_{gg'}^{\chi_m}}{\sigma_{gg'}^{old} - \sigma_{gg'}^{\chi_m}} \sum_{\substack{i=1\\ i\neq m}}^{n} \sigma_{gg'}^{\chi_i} + \alpha_{gg'}^{m}\sigma_{gg'}^{\chi_m} \\ &= \sigma_{gg'}^{old} - \alpha_{gg'}^{m}\sigma_{gg'}^{\chi_m}[1-1] \\ &= \sigma_{gg'}^{old} ,\end{aligned}$$

where

$$\sigma_{gg'}^{old} - \sigma_{gg'}^{\chi_m} = \sum_{\substack{i=1\\ i\neq m}}^{n} \sigma_{gg'}^{\chi_i} .$$

IV.B.1.b. Direct Variation Approach

One can proceed by applying variation factors $\beta_{gg'}$ to the total SED instead of applying these factors to the cross sections of the excitation levels involved. This can be seen by noticing that

$$\begin{aligned}\sigma_{gg'}^{new} &= \sigma_{gg'}^{old}\left[1 + \left(\sum_{\substack{i=1\\ i\neq m}}^{n} \alpha_g^i\sigma_{gg'}^{\chi_i} + \alpha_m\sigma_{gg'}^{\chi_m}\right) \times \frac{1}{\sigma_{gg'}^{old}}\right] \\ &= \sigma_{gg'}^{old}\left[1 + \left(\sum_{i=1}^{n} \alpha_g^i\sigma_{gg'}^{\chi_i}\right) \times \frac{1}{\sigma_{gg'}^{old}}\right] \\ &= \sigma_{gg'}^{old}[1 + \beta_{gg'}^{m}] , \end{aligned} \quad (13)$$

where the variation factor $\beta_{gg'}^{m}$ is now given by

$$\beta_{gg'}^{m} = \left(\sum_{i=1}^{n} \alpha_g^i\sigma_{gg'}^{\chi_i}\right) \times \frac{1}{\sigma_{gg'}^{old}} . \quad (14)$$

The condition that σ_g^{new} should be the same as σ_g^{old} leads to

$$\sum_{g'} \sigma_{gg'}^{old}\beta_{gg'}^{m} = \sum_{i=1}^{n} \alpha_g^i\sigma_g^{\chi_i} = 0 . \quad (15)$$

In this treatment, the $\beta_{gg'}$ factors are derived from Eq. (15), depending on the variation factor of the prime level χ_m and the variation factors for the other levels. However, in practice, one can increase the cross section $\sigma_{gg'}^{old}$ by an assumed factor $\beta_{gg'}^{m}$ for a specified exit energy range m; meanwhile, the cross section $\sigma_{gg'}^{old}$ for other possible exit energy ranges i is decreased such that the total cross section σ_g remains the same. Thus, from Eq. (13), we have

$$\sigma_{gg'}^{new} = \begin{cases} \sigma_{gg'}^{old}(1 + \beta_{gg'}^{m}) , & g' \text{ is in the } m\text{'th interval} \\ \sigma_{gg'}^{old}(1 + \beta_{gg'}^{i}) , & g' \text{ is not in the } m\text{'th interval} . \end{cases}$$

The condition that σ_g^{new} should be the same as σ_g^{old} leads to

$$\sum_{g'} \sigma_{gg'}^{new} = \sum_{g'} \sigma_{gg'}^{old}(1 + \beta_{gg'}^{m} + \beta_{gg'}^{i})$$

and

$$\sigma_g^{new} = \sigma_g^{old} + \sum_{g'} \sigma_{gg'}^{old}(\beta_{gg'}^{m} + \beta_{gg'}^{i}) .$$

Therefore, we have

$$\sum_{g'} \sigma_{gg'}^{old}\beta_{gg'}^{m} = -\sum_{g'} \sigma_{gg'}^{old}\beta_{gg'}^{i} . \quad (16)$$

In this case, the factors $\beta_{gg'}^{i}$ are not calculated from the level variation factors α_g^i described earlier.

IV.B.2. Variation in the Secondary Angular Distribution

The importance of studying the effect of variations in the SAD from the ^{9}Be$(n,2n)$ multiplying reaction on the design parameter at hand stems from the fact that beryllium is normally placed in front of the tritium breeding zone in a fusion blanket. An overestimation in the neutrons scattered in the forward direction from the ^{9}Be$(n,2n)$ reaction could lead to an overestimation of local TPRs behind the beryllium layer. The reverse is true if neutrons are overestimated in the backward direction. The course followed in examining the sensitivity of local TPRs to variations in the SAD of neutrons emitted from the ^{9}Be$(n,2n)$ reaction is to adopt a Legendre expansion of the cross section of these reactions whose coefficients could be varied to reflect a particular perturbation in the SAD. One can then assume that the space of the scattering angle is partitioned into three regions: forward, upward, and backward. These regions are defined as region 1 ($0.5 < \mu < 1.0$), region 2 ($-0.5 < \mu < 0.5$), and region 3 ($-1.0 < \mu < -0.5$), where μ is the cosine of the scattering angle in the laboratory system. In this analysis, the P_3 approximation is used to represent the scattering cross section at a particular angle μ. That is,

$$\begin{aligned}\sigma_{gg'}(\mu) &\cong \sigma_{gg'}^{0} + \sigma_{gg'}^{1}P_1(\mu) + \sigma_{gg'}^{2}P_2(\mu) + \sigma_{gg'}^{3}P_3(\mu) \\ &= \sigma_{gg'}^{0} + \sigma_{gg'}^{1}(\mu) + \sigma_{gg'}^{2}\frac{(3\mu^2 - 1)}{2} \\ &\quad + \sigma_{gg'}^{3}\frac{(5\mu^3 - 3\mu)}{2} . \end{aligned} \quad (17)$$

By integrating the angular cross section over the three regions defined earlier and over the entire angular space, we get

$$I_{gg'_1} = \int \sigma_{gg'}(\mu)\, d\mu \quad (0.5 < \mu < 1.0) ,$$

$$I_{gg'_2} = \int \sigma_{gg'}(\mu)\, d\mu \quad (-0.5 < \mu < 0.5) ,$$

$$I_{gg'_3} = \int \sigma_{gg'}(\mu)\, d\mu \quad (-1.0 < \mu < -0.5) ,$$

and

$$I_{gg'_t} = \int \sigma_{gg'}(\mu)\, d\mu \quad (-1.0 < \mu < 1.0) .$$

Here, we have

$$I_{gg'_t} = I_{gg'_1} + I_{gg'_2} + I_{gg'_3} , \tag{18}$$

and to preserve the SAD, the condition

$$I_{gg'_t} = \text{constant} \tag{19}$$

should hold. This implies no variation in the P_0 component of the cross section $\sigma^0_{gg'}$. Performing these integrations, we get

$$\begin{bmatrix} 4a & 0 & 0 & 0 \\ a & b & c & d \\ 2a & 0 & -2c & 0 \\ a & -b & c & -d \end{bmatrix} \cdot \begin{bmatrix} \sigma^0_{gg'} \\ \sigma^1_{gg'} \\ \sigma^2_{gg'} \\ \sigma^3_{gg'} \end{bmatrix} = \begin{bmatrix} I_{gg'_t} \\ I_{gg'_1} \\ I_{gg'_2} \\ I_{gg'_3} \end{bmatrix} , \tag{20}$$

where a, b, and c are constants. Figure 7 shows the variations assumed in this study in the SAD. From Eq. (20), if we increase $I_{gg'_1}$ by a factor α_m, $\sigma^1_{gg'}$ will be increased by a factor $\chi_{gg'_1}$ expressed as

$$\chi_{gg'_1} = \frac{I_{gg'_1}(\alpha_m)}{b \cdot \sigma^1_{gg'}} , \tag{20a}$$

with the assumption that $\sigma^3_{gg'}$, $\sigma^2_{gg'}$, and $I_{gg'_2}$ do not change. This is the "forward" variation considered here. If we increase $I_{gg'_2}$ by a factor α_m, $\sigma^2_{gg'}$ will be increased by a factor $\chi_{gg'_2}$ expressed as

$$\chi_{gg'_2} = \frac{I_{gg'_2}(\alpha_m)}{-2c \cdot \sigma^2_{gg'}} , \tag{20b}$$

and the conservation condition expressed by Eq. (19) necessitates that no change in $\sigma^1_{gg'}$ and $\sigma^3_{gg'}$ takes place (upward variation). If we increase $I_{gg'_3}$ by a factor α_m, $\sigma^1_{gg'}$ will be increased by a factor $\chi_{gg'_1}$ expressed as

$$\chi_{gg'_1} = \frac{I_{gg'_3}(\alpha_m)}{-b \cdot \sigma^1_{gg'}} \tag{20c}$$

with the assumption that $\sigma^3_{gg'}$, $\sigma^2_{gg'}$, and $I_{gg'_2}$ do not change (backward variation).

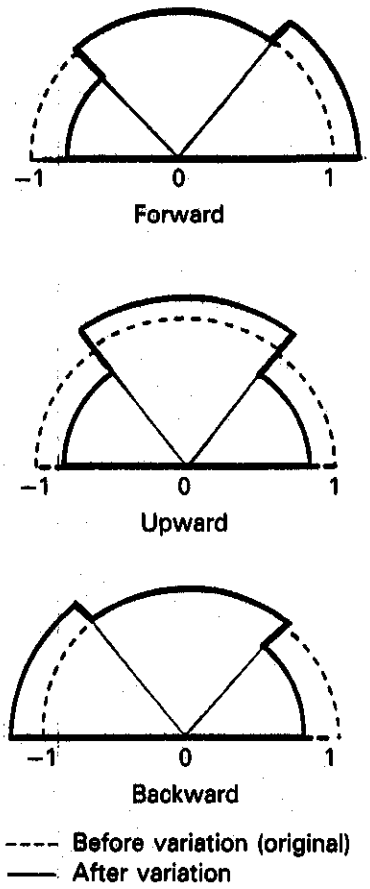

Fig. 7. Three different variations considered in the SAD analysis: (a) forward, (b) upward, and (c) backward.

IV.B.3. Sensitivity Profiles for SED and SAD

In general, the relative sensitivity profile $P_{\Sigma_x}(E)$ is defined as the percentage change in the integrated parameter R under consideration (T_6 or T_7 in our case) due to a 1% increase in a particular type of cross section Σ_x at energy E, and this variation is assumed to take place within a particular region in space. This coefficient is given by

$$P_{\Sigma_x}(E) = -\frac{1}{R} \langle \phi^*, L_{\Sigma_x} \phi \rangle_E , \tag{21}$$

where ϕ and ϕ^* are the forward and the adjoint angular flux, and they are the solutions of the transport equations $L\phi = S$ and $L^*\phi^* = \Sigma_r$, respectively; L_{Σ_x} is the part of the Boltzmann operator that includes the perturbed cross section Σ_x. The notation $\langle\ ,\ \rangle_E$ indicates integration over the phase-space $\mathbf{\Omega}$, and $\boldsymbol{r}$ only, while the notation $\langle\ ,\ \rangle$ indicates integration over the whole phase-space $\mathbf{\Omega}$, $\boldsymbol{r}$, and E. The perturbation theory used to derive Eq. (21) can be found in Refs. 37 through 43.

In the multigroup treatment, and based on the excitation level approach discussed earlier, the relative sensitivity profile for variation in the cross section of an excitation level i is given by

$$P^g_{\Sigma^i_x}(\text{SED}) = \frac{4\pi}{R\Delta U^g}\left[\sum_{g'=g}^{G_{max}}\sum_{l=0}^{L_{max}}(2l+1)\alpha^l_g\Sigma^{\chi_{ig}\to g'}_{\Sigma^i_l} \times \sum_{k=0}^{l}\sum_{j=1}^{J_{mesh}} V_j\phi^{kg}_l(j)\phi^{*kg}_l(j) - \sum_{l=0}^{L_{max}}(2l+1)\alpha^l_g\Sigma^{\chi_{ig}}_{x_T} \times \sum_{k=0}^{l}\sum_{j=1}^{J_{mesh}} V_j\phi^{kg}_l(j)\phi^{*kg}_l(j)\right] . \quad (22)$$

The first term is the "scattering gain" term, and the second is the "collisional loss" term. The total relative sensitivity profile for SED is the summation of all the excitation levels' sensitivity coefficients and is given by

$$P^g_{\Sigma_x}(\text{SED}) = \sum_{i=1}^{n} P^g_{\Sigma^i_x}(\text{SED}) = \frac{4\pi}{R\Delta U^g}\left\{\sum_{i=1}^{n}\left[\sum_{g'=g}^{G_{max}}\sum_{l=0}^{L_{max}}(2l+1)\alpha^l_g\Sigma^{\chi_{ig}\to g'}_{\Sigma^i_l} \times \sum_{k=0}^{l}\sum_{j=1}^{J_{mesh}} V_j\phi^{kg}_l(j)\phi^{*kg}_l(j) - \sum_{l=0}^{L_{max}}(2l+1)\alpha^l_g\Sigma^{\chi_{ig}}_{x_T} \times \sum_{k=0}^{l}\sum_{j=1}^{J_{mesh}} V_j\phi^{kg}_l(j)\phi^{*kg}_l(j)\right]\right\} , \quad (23)$$

where

V_j = volume of spatial mesh j

ΔU^g = lethargy width of energy group g

G_{max} = maximum number of energy groups used in the multigroup calculations

L_{max} = maximum number of polynomials used in the P_l approximation

$\phi^{kg}_l, \phi^{*kg}_l$ = forward and adjoint flux component of the associated Legendre polynomials.

Note that the second term of the SED sensitivity profile will be cancelled out [see Eq. (5)] because the total cross section was kept the same when the SED was varied. Thus, the SED sensitivity profile can be rewritten as

$$P^g_{\Sigma_x}(\text{SED}) = \frac{4\pi}{R\Delta U^g}\left[\sum_{i=1}^{n}\sum_{g'=g}^{G_{max}}\sum_{l=0}^{L_{max}}(2l+1)\alpha^l_g\Sigma^{\chi_{ig}\to g'}_{\Sigma^i_l} \times \sum_{k=0}^{l}\sum_{j=1}^{J_{mesh}} V_j\phi^{kg}_l(j)\phi^{*kg}_l(j)\right] . \quad (24)$$

However, in the direct variation treatment, the variation factors $\beta^l_{gg'}$ and $\beta^m_{gg'}$ could be applied to the old SED distribution. In this case, the SED sensitivity profile is given by

$$P^g_{\Sigma_x}(\text{SED}) = \frac{4\pi}{R\Delta U^g}\sum_{i=1}^{n}\sum_{g'=g}^{G_{max}}\sum_{l=0}^{L_{max}}(2l+1)\beta^i_{gg'}\Sigma^{g\to g'}_{\Sigma^i_l} \times \sum_{k=0}^{l}\sum_{j=1}^{J_{mesh}} V_j\phi^{kg}_l(j)\phi^{*kg}_l(j) , \quad (25)$$

where n is the number of exit energy ranges considered in the old distribution. Likewise, the sensitivity profiles for the SAD can be obtained by using the variation factors $\chi_{gg'_i}$ discussed in Sec. IV.B.2 in a similar fashion. The three scattering regions considered in this analysis are

$$P^{forward}_g(\text{SAD}) = -\sum_{g'=g}^{G_{max}}\frac{1}{R}\langle\phi^*, \chi^{forward}_{gg'_1}L_{\Sigma_{gg'_1}}\phi\rangle_{g'} ,$$

$$P^{upward}_g(\text{SAD}) = -\sum_{g'=g}^{G_{max}}\frac{1}{R}\langle\phi^*, \chi^{upward}_{gg'_2}L_{\Sigma_{gg'_2}}\phi\rangle_{g'} ,$$

and

$$P^{backward}_g(\text{SAD}) = -\sum_{g'=g}^{G_{max}}\frac{1}{R}\langle\phi^*, \chi^{backward}_{gg'_1}L_{\Sigma_{gg'_1}}\phi\rangle_{g'} . \quad (26)$$

IV.C. Calculation Procedures

The cross sections needed for the forward and the adjoint transport calculations were generated from the DLC-113/VITAMIN-E master interface fine-group library[44] (174 groups), using the CHOX and MALOCS codes of the AMPX processing system[32] and from the MATXS5 multigroup cross-section file by using the TRANSX-CTR program.[31] These 30-group transport forward and adjoint cross-section libraries were converted to group-organized cross-section sets by using the GIP code.

The total and partial cross sections for the sensitivity analysis were also prepared from the VITAMIN-E master library into the 30-group structure by using the NITAWL module of the AMPX processing system. The ANISN-formatted transfer matrices of the total and partial cross-section libraries were converted to the MATXS format, which is required for the sensitivity analysis by using the ANTMX code of the FORSS cross-section sensitivity/uncertainty analysis system.[45] This code system was developed at Oak Ridge National Laboratory and is applied in this analysis. However,

some modifications in that system were required. The calculational procedures are summarized in Fig. 8.

The unshaded boxes in Fig. 8 represent the calculational procedures and codes used to perform the sensitivity/uncertainty analysis for the "smooth" cross sections, and the shaded boxes indicate the calculational path followed in carrying out the sensitivity and uncertainty analysis for the SED and SAD variations. As shown, some modifications were required in the modules of the FORSS code to perform the SED and SAD sensitivity/uncertainty analysis. The volume-integrated product code, VIP, was used for the preparation of the $\langle \phi_K, \phi^* \rangle$ flux file in two-dimensional form. This code was developed by Childs and co-workers[45-47] and is used for each response considered in this analysis. The MATXS partial cross sections and the volume-integrated flux file $\langle \phi_K, \phi^* \rangle$ were used as input to the JULIET code to get the sensitivity profiles for each partial cross section. The end product of the JULIET sensitivity profiles are placed in a SENPRO file. For the SED/SAD analysis, after the variation factor for each excitation level was calculated by the VARIX code, these factors were applied to each sensitivity profile generated by the JULIX code, a modified version of JULIET.

The sensitivity profiles were coupled to the cross-section uncertainty information (quantified in terms of RSDs) contained in ENDF/B-V, file 33. For beryllium smooth cross sections, the uncertainty information was

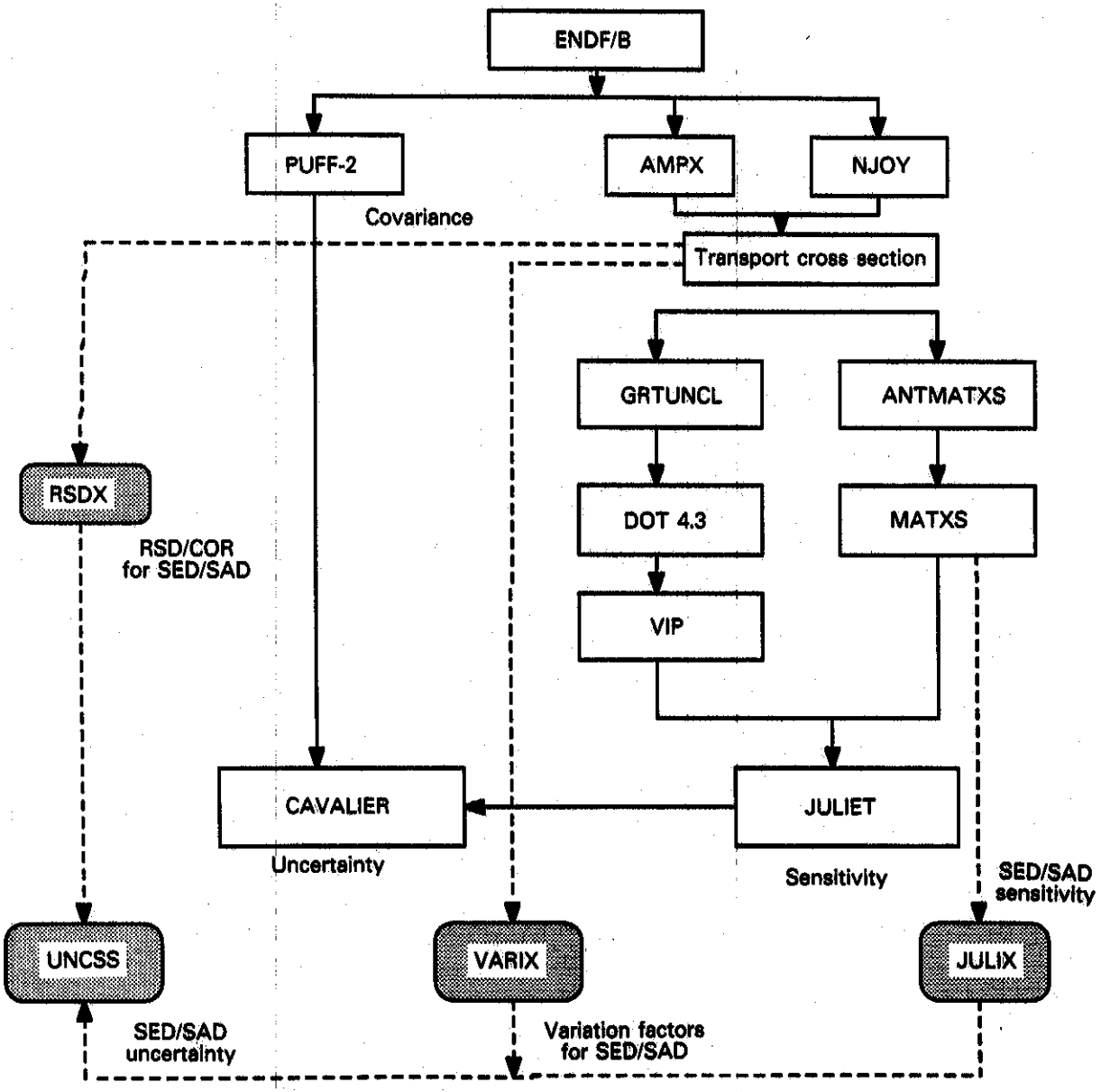

Fig. 8. Calculational procedures of the FORSS SED and SAD sensitivity/uncertainty analysis.

obtained from the LANL evaluation (the only existing cross-section uncertainty information for beryllium). For the uncertainties in the SED and SAD of the $^9Be(n,2n)$ cross section, they were derived from a simple comparison for the transfer cross section $\sigma_{gg'}$ of the $^9Be(n,2n)$ transfer cross-section matrices of the three evaluations for beryllium in the manner described in Sec. VI.B.2. The RSDX code was developed to generate the RSD in the $\sigma_{gg'}$ of the $^9Be(n,2n)$ cross section from the three evaluations, and the UNCSS was developed to couple sensitivity profiles to uncertainty data. The PUFF code was used to generate the covariance matrices for smooth cross sections, as shown in Fig. 8.

The BES system discussed in Sec. III was selected for the analysis. Five locations (denoted P1, P2, P3, P4, and P5 at 2.54, 6.72, 8.22, 10.72, and 35.72 cm from the front surface of the Li_2O assembly) were selected for each T_6 and T_7, as shown in Fig. 9. Locations P2 and P3 are inside the beryllium zone, location P3 is 0.72 cm behind it, and P5 is in the middle zone of the Li_2O assembly.

One forward calculation was performed using the DOT 4.3 code[48] in two-dimensional r-z geometry along with the uncollided flux obtained by the GRTUNCL code.[49] The calculations were performed using the P_5-S_8 approximation with the 30-group neutron library. Ten adjoint calculations were needed (five for T_6 and five for T_7) to calculate the adjoint fluxes. The response function [$^6Li(n,\alpha)t$ or $^7Li(n,n'\alpha)t$ macroscopic cross sections] was considered at each location, separately, as the source to the adjoint equation, and the adjoint fluxes (ϕ_6^* and ϕ_7^*) were calculated using an adjoint cross-section library generated by using the GIP code. Note that the uncollided adjoint fluxes were first generated by the GRTUNCL code since the responses considered are at spatial points in space.

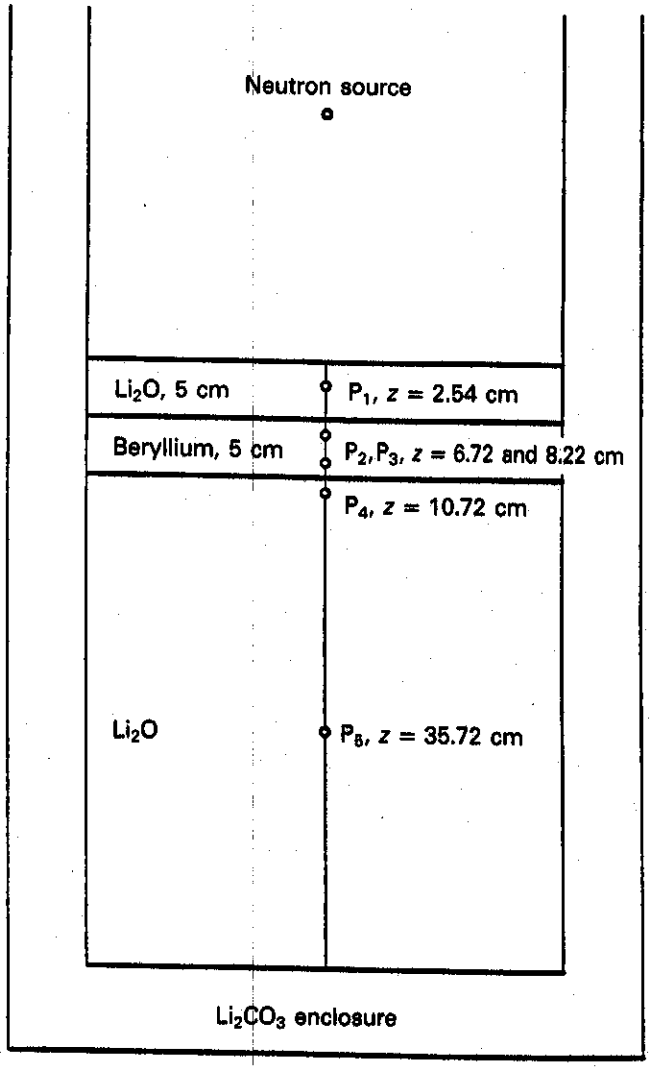

Fig. 9. Different detector locations considered in the sensitivity/uncertainty analysis for the BES system.

V. SENSITIVITY/UNCERTAINTY ANALYSIS RESULTS

V.A. Sensitivity Analysis Results

V.A.1. Sensitivity Analysis Results for the SED of the $^9Be(n,2n)$ Cross Section

V.A.1.a. Excitation Level Variations

The results given here consider the LANL evaluation although parallel analyses were carried out for the ENDF/B-V and LLNL evaluations. The LANL evaluation was based on data for a cluster of real levels near $E_{th} = 2.43$ MeV and 32 excitation energy bins, with a half-width of 0.25 MeV, to represent the $(n,2n)$ continuum levels as mentioned earlier. In this analysis, these levels were grouped into three "lumped" levels that each consisted of nine pseudolevels. Details of the pseudolevel groups are given in Table I. The required variation factors for the level-independent and the level-dependent treatments are obtained from Eqs. (7) and (10); then, these factors are used to calculate the total integrated relative sensitivity coefficients shown in Fig. 10 for T_6 at the five locations P1 through P5. As shown, the coefficients corresponding to the first

TABLE I

Grouping into Three Lumped Excitation Levels in the LANL Evaluation for the $^9Be(n,2n)$ Cross Section

Lumped Level	Pseudolevel	E_{th} (MeV)
1	1 through 9	2.25
2	10 through 18	6.75
3	19 through 27	11.25

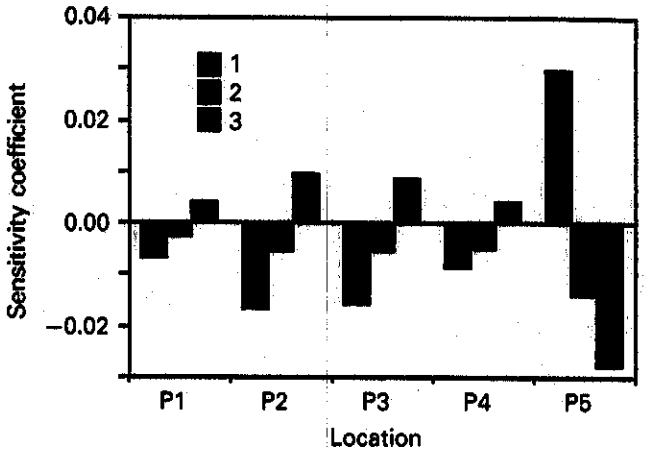

Fig. 10. Integrated sensitivity coefficient for T_6 due to variation in the SED of the $^9Be(n,2n)$ cross section (level-independent treatment): LANL evaluation.

excitation level (χ_1) [i.e., when the prime level considered is χ_1; see Eq. (7)] and the second excitation level (χ_2) are negative inside and around the beryllium layer while the coefficients corresponding to the third excitation level (χ_3) are positive. This is because the low-energy component of the total SED is emphasized (i.e., increased) in the case of the third excitation level. Note that the SED for three lumped excitation levels from the 33 pseudolevels is a distribution of the two neutrons emitted from the $^9Be(n,2n)$ reaction. Figure 11 shows this SED ($\sigma_{gg}^{\chi_l}$, not normalized) for each lumped excitation level. If the incident neutron energy is ~14 MeV, the two neutrons emitted from exciting the third excitation level will have energy of ~1 MeV, an important range for contributing to T_6, while for the first and second excitation levels, the two neutrons emitted will have energies of ~10 and 5 MeV, respectively, ranges that are not largely contributing to T_6.

As for T_7, increasing the cross section of the first excitation level while decreasing the cross sections of the other levels [to keep the integrated $^9Be(n,2n)$ cross section the same] leads to an increase in T_7 at all locations. This is because the high-energy component of the total SED is emphasized (i.e., increased). The coefficients for the second and third levels are negative, as shown in Fig. 12. The treatment with either the level-dependent or the level-independent approach gives similar results (not shown). The integrated relative sensitivity coefficients for the variations in the various levels are large (by about an order of magnitude) for T_7 as compared with the coefficients for T_6, although in both cases, the absolute values of these coefficients are small.

The choice of which excitation level to increase (or decrease) with a compensating decrease (or increase) in the other levels depends on the discrepancies between measurements and calculations. For example,

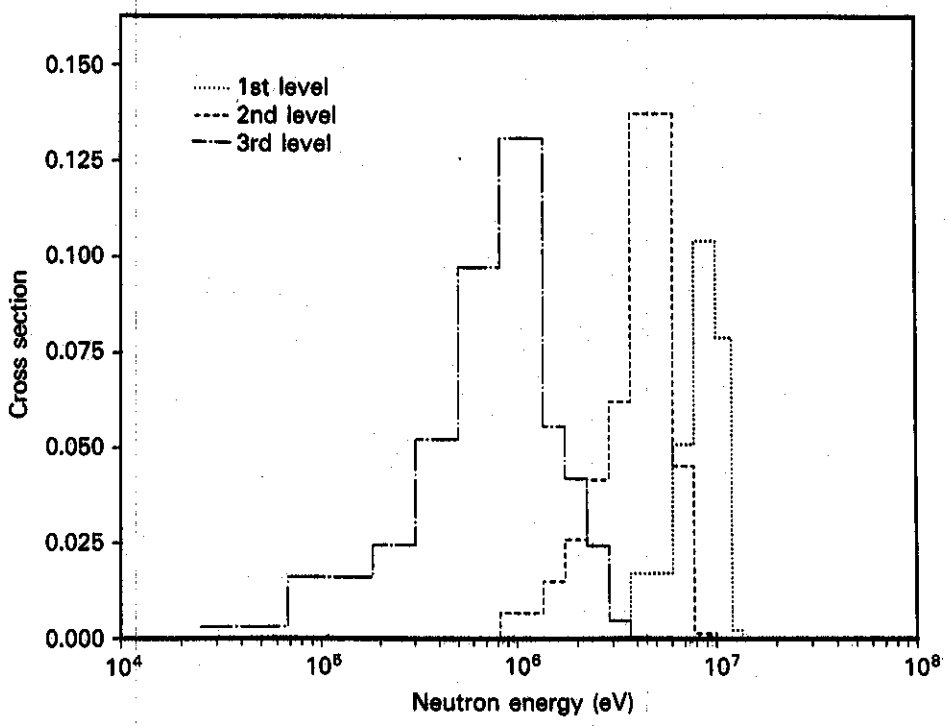

Fig. 11. The $^9Be(n,2n)$ total cross section from three levels of the LANL evaluation for the $^9Be(n,2n)$ cross section (E_{ln} = 13.5 to 15 MeV).

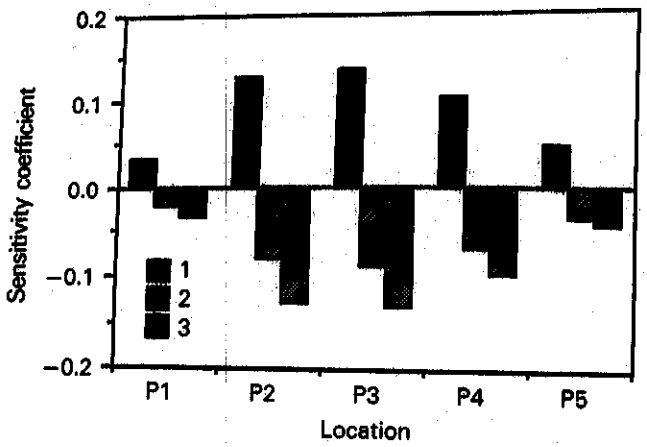

Fig. 12. Integrated sensitivity coefficients for T_7 due to variation in the SED of the $^9Be(n,2n)$ cross section (level-independent treatment): LANL evaluation.

choosing the third excitation level in the LANL evaluation will improve the C/E values for T_6 (lower than unity) just behind the beryllium layer in the experiment at hand. However, the sensitivity coefficient for a 1% increase in that level is ~0.01% for T_6 at location P4. The observed discrepancy of ~5 to 10% shown in the Fig. 1 variation cannot be explained by the 1% variation assumed, unless this variation is 100% or more. It was shown, however, that when the uncertainty information is coupled with the sensitivity coefficients, large uncertainties in T_6 (and T_7) are obtained (see Sec. V.B.2).

V.A.1.b. Direct Variation in the SED of the $^9Be(n,2n)$ Cross Section over Several Energy Intervals

The sensitivity coefficients were calculated according to Eqs. (15) and (23) for the direct variations in the SED of the LANL $^9Be(n,2n)$ cross section. The direct variations were selected to conform with some of the discrepancies between the calculations and measurements in recent experiments. For example, the results of Oyama and Maekawa's experiment[17] on the leakage spectrum behind a 5-cm-thick beryllium slab with LANL data showed that the calculated spectrum is underestimated in the energy range $0.1 < E_{out} < 0.5$ MeV, overestimated in the energy range $0.5 < E_{out} < 10$ MeV, and underestimated in the energy range $E_{out} > 10$ MeV.

Two types of direct variation in the SED of the $^9Be(n,2n)$ cross section were performed by *assuming* that these discrepancies were due to the inadequacy of the SED of the total $^9Be(n,2n)$ cross section. In case 1, the overestimated part of the integrated spectrum ($0.5 < E_{out} < 10$ MeV) was decreased by 1%, and the necessary increase in the underestimated parts ($E_{out} > 10$ MeV and $0.1 < E_{out} < 0.5$ MeV) was calculated such that the total integrated spectrum was kept the same. The variations were also assumed to be for all incident energies [above the threshold energy of the $^9Be(n,2n)$ reaction]. In case 2, the lower energy part of the SED below 0.1 MeV was increased by 1%, and the necessary decrease in the SED above 0.1 MeV was carried out for all incident energies to investigate the effect of a variation in the lower energy tail of the SED of the $^9Be(n,2n)$ reaction on T_6.

The integrated sensitivity coefficients resulting from these variations are shown in Fig. 13. In case 1, the integrated coefficients are positive for T_6 inside and around the beryllium layer. Since T_6 is increased behind this layer, the drop in the C/E curves observed at this location will be lessened. However, the coefficients are still small in absolute values. The breakdown of the contribution to the sensitivity coefficients of T_6, at each location, that comes from various energy ranges, namely, $10 < E_{out} < 17$ MeV, $0.5 < E_{out} < 10$ MeV, and $0.1 < E_{out} < 0.5$ MeV, is shown in Fig. 14. No variation in the SED was carried out below 0.1 MeV in case 1. The 1% decrease in the energy range $0.5 < E_{out} < 10$ MeV resulted in a negative (and relatively large) contribution to the sensitivity coefficients for T_6 at all locations. However, the contributions from the necessary increase in the SED above 10 MeV and in the energy range $0.1 < E_{out} < 0.5$ MeV (which is also relatively large) compensate for the negative contribution resulting from the decrease in SED in the energy range $0.5 < E_{out} < 10$ MeV. The net result is positive coefficients inside the beryllium layer and around it. Note that this net coefficient is negative at the bulk of the Li_2O zone (location P5).

In case 2, the integrated sensitivity coefficients for T_6 were also positive inside and around the beryllium

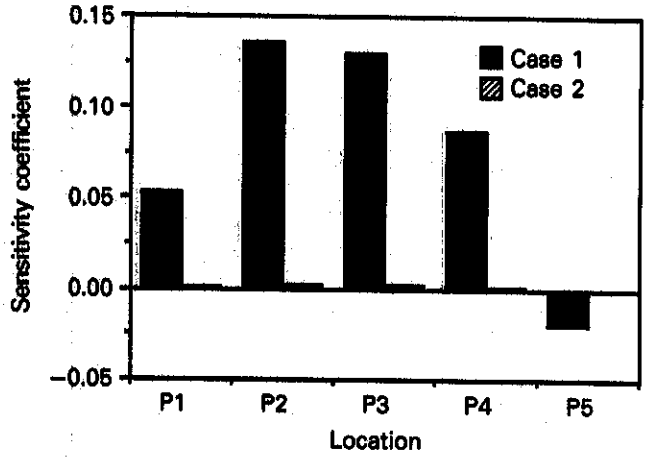

Fig. 13. Integrated sensitivity coefficient for T_6 due to two types of variations in the SED of the $^9Be(n,2n)$ cross section (direct variation).

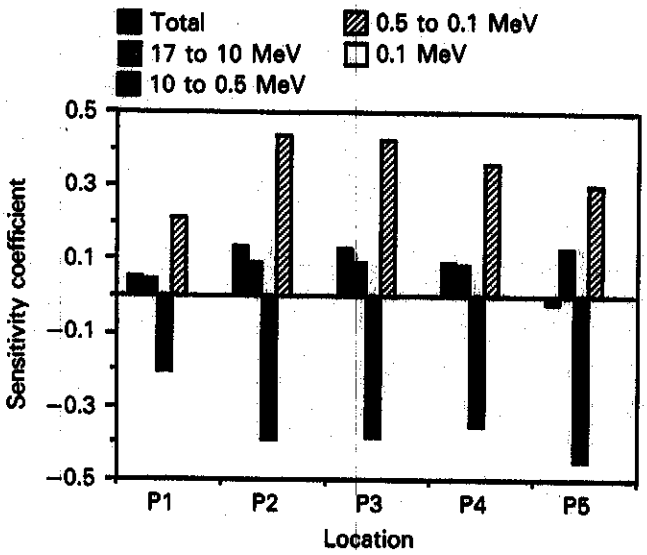

Fig. 14. Breakdown (by energy range) in the integrated sensitivity coefficient for T_6 due to case 1 variation in the SED of the $^9Be(n,2n)$ cross section.

layer, as shown in Fig. 13. However, their absolute values are very small (0.001%). Therefore, variations in the SED of the emitted neutrons from the $^9Be(n,2n)$ reaction below 0.1 MeV have little effect on T_6; the larger effect is due to variations performed above 0.1 MeV, as in case 1.

As for T_7, the variation in case 1 indicates that T_7 has positive integrated sensitivity coefficients at all locations, and their absolute values increase as one proceeds toward the back locations of the test assembly (not shown). Although the SED was decreased (by 1%) in the energy range $0.5 < E_{out} < 10$ MeV, where the threshold of the $^7Li(n,n'\alpha)t$ reaction lies, the increase in the SED above 10 MeV leads to a larger and positive contribution to the total sensitivity coefficient, and that leads to net positive values. Therefore, any uncertainties in the SED of the $^9Be(n,2n)$ reaction above 10 MeV will have a large effect on T_7, as expected.

V.A.2. Sensitivity Analysis Results for the SAD of the $^9Be(n,2n)$ Cross Section

The SAD was increased by 1% in the interval $0.5 < \mu < 1$ for the first case (forward variation). The upward SAD ($-0.5 < \mu < 0.5$) was kept unchanged. The required change in the backward SAD ($-1.0 < \mu < -0.5$) was calculated such that the integrated SAD was kept the same. In the second case (upward variation), a 1% increase in the upward SAD was applied with a corresponding decrease in the forward and backward SADs. In the third case, the backward SAD was increased by a 1% (backward variation), and the required change in the forward SAD was calculated such that the integrated SAD was kept the same. The upward SAD remained unchanged in this case. The variation factors for each SAD variation were obtained by Eqs. (20a), (20b), and (20c) and used in the SAD sensitivity calculations by applying Eqs. (26).

The integrated sensitivity coefficients for T_6 are shown in Fig. 15 for the three cases. The coefficients of T_6 for the forward variation in the SAD is positive inside and behind the beryllium layer (0.009 and 0.013%, respectively) but negative in the front Li_2O zone, as expected. These coefficients increase as one proceeds inside the back Li_2O zone because more neutrons can now reach these locations and contribute to T_6. The sensitivity coefficients of T_7 for the forward variation are negative inside the beryllium layer and at the front Li_2O layer, but positive (with increasing trend) behind the beryllium layer, as shown in Fig. 16,

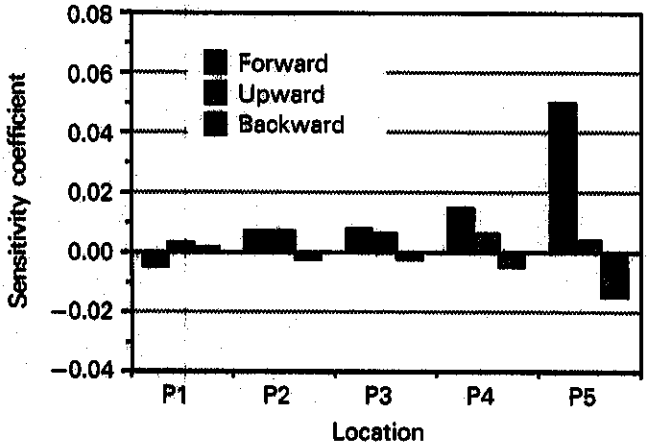

Fig. 15. Integrated sensitivity coefficient for T_6 due to three types of variations in the SAD of the $^9Be(n,2n)$ cross section: LANL evaluation.

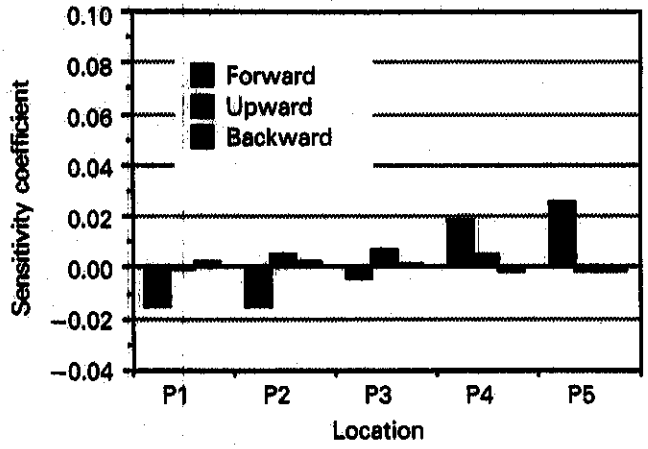

Fig. 16. Integrated sensitivity coefficient for T_7 due to three types of variations in the SAD of the $^9Be(n,2n)$ cross section: LANL evaluation.

because more high-energy neutrons reach the bulk of the back Li_2O zone. The coefficients for the upward variation are always positive and large inside the beryllium layer because more neutron multiplication occurs. However, as a result of the softening of the incident spectrum with this type of variation, the high-energy neutrons reaching the back Li_2O zone are decreased, and hence, a reduction in T_7 occurs in the bulk of the Li_2O zone. The coefficients for the backward variation are positive (but small) inside the beryllium layer and at the front Li_2O layer but negative behind the beryllium layer, as expected.

V.A.3. Variations in the Other Cross Sections of Beryllium

The sensitivity analysis was extended to include variations in the other smooth integrated partial cross sections of beryllium to study their effects on T_6 and T_7. The analysis was carried out for the three evaluations for beryllium.

The integrated sensitivity coefficients for T_6 increase inside and around the beryllium layer when the $^9Be(n,total)$ cross section is increased, as shown in Fig. 17. The sensitivity coefficients due to a 1% increase in the $^9Be(n,total)$ cross section are ~3.1 to 3.3% inside and ~0.95% behind the beryllium layer (location P4). An increase in the $^9Be(n,total)$ cross section means an increase in the $(n,elastic)$ and $(n,2n)$ reactions, thus leading to more neutron moderation and multiplication; therefore, enhancement in T_6 occurs near the beryllium layer. However, the contribution from the $^9Be(n,elastic)$ reaction dominates that from the $^9Be(n,2n)$ reaction inside and around the beryllium layer. This is seen from Fig. 18, where the sensitivity coefficients for the $^9Be(n,elastic)$ cross section are shown.

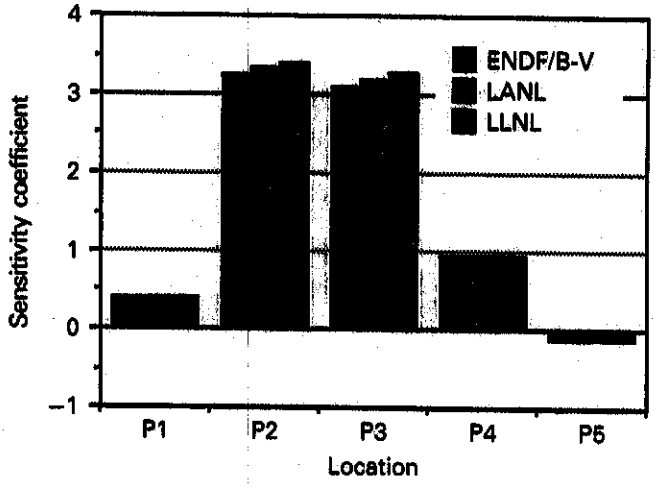

Fig. 17. Integrated sensitivity coefficient for T_6 due to a 1% increase in the total cross section of beryllium.

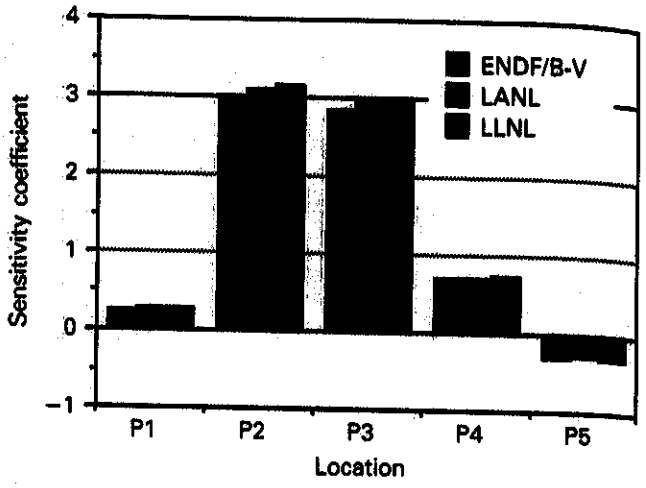

Fig. 18. Integrated sensitivity coefficient for T_6 due to a 1% increase in the elastic cross section of beryllium.

The values (and signs) of the sensitivity coefficients due to variation in the $^9Be(n,total)$ cross section are basically driven by the contribution from the $^9Be(n,elastic)$ cross section (~90% of the contribution inside the beryllium layer). The contribution from the $^9Be(n,2n)$ cross section is small (~9%) inside the beryllium layer but increases just behind that layer (~20%). The sensitivity coefficients behind the beryllium layer for variations in the total $^9Be(n,2n)$ cross section are factors of ~3 and ~25 larger than those obtained from variations in the SED and SAD, respectively. However, at locations deep inside the Li_2O zone (location P5), the coefficient for the $^9Be(n,total)$ cross section [basically due to $^9Be(n,elastic)$ reactions] are negative since high-energy neutrons reaching this location decrease with increasing a number of interactions (particularly elastic ones) inside the beryllium layer. The sensitivity profiles for T_6 for variations in the $^9Be(n,elastic)$ cross section are shown in Fig. 19. This figure shows in what energy range (or group) the variation in the cross section will give the largest coefficient. As shown, variations in the low-energy range for the $^9Be(n,elastic)$ cross section lead to a large variation in T_6, particularly inside and just behind the beryllium layer. Note also that the profiles are negative at deep locations (location P5).

The sensitivity coefficients for T_7 due to a 1% increase in the $^9Be(n,total)$ cross section are always negative at all locations, and they are driven by the variation in the $^9Be(n,2n)$ cross section (see Fig. 20). The coefficients for the $^9Be(n,elastic)$ cross section are an order of magnitude lower than those of the $^9Be(n,2n)$ cross section inside the beryllium layer. The sensitivity profiles of T_7 due to variations in the $^9Be(n,2n)$ cross sections are negative at all locations (not shown), and T_7 is most sensitive to variation in the $^9Be(n,2n)$ cross section at incident group 2 (13.5 to 15 MeV).

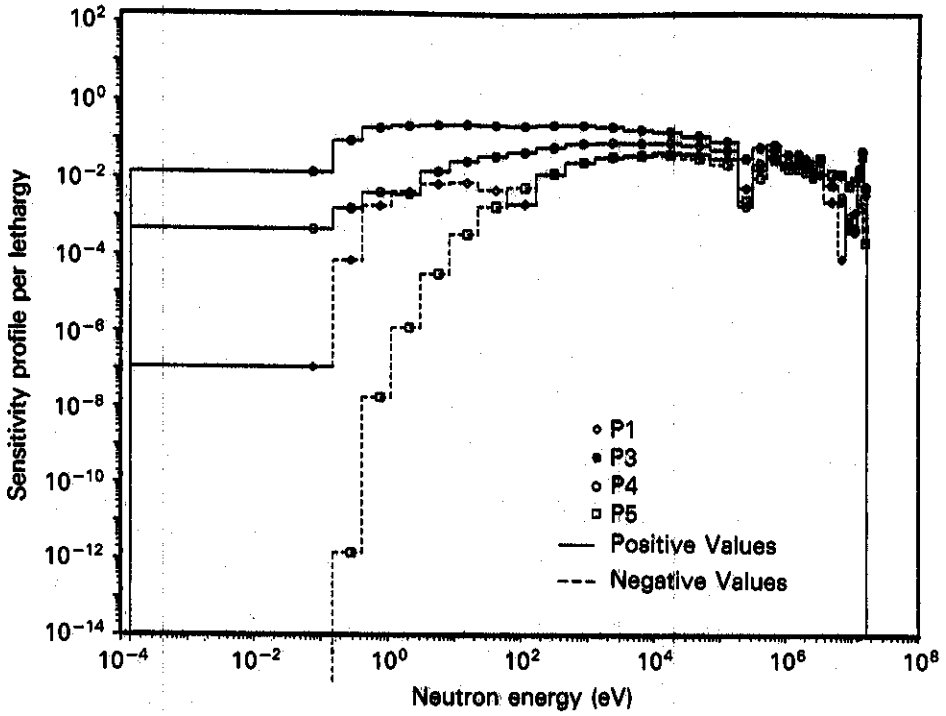

Fig. 19. Relative sensitivity profile of T_6 due to a 1% increase in the ^{9}Be(n,elastic) cross section at various locations.

V.A.4. Variations in the Cross Sections of Other Materials

The integrated sensitivity coefficients for T_6 due to a 1% increase in the total cross sections of other materials are shown in Fig. 21. Inside and around the beryllium layer, the coefficients of beryllium are the largest. The second largest (and positive) coefficients at these locations are those for ^{16}O, and they are mainly due to variations in the elastic and inelastic cross sections whose reactions tend to slow down neutrons to lower energy ranges where T_6 is large. The contribution from the ^{16}O(n,elastic) cross section is dominant. This can be seen from Fig. 22, which shows the contribution to the total sensitivity coefficient from variations in each partial cross section at various locations,

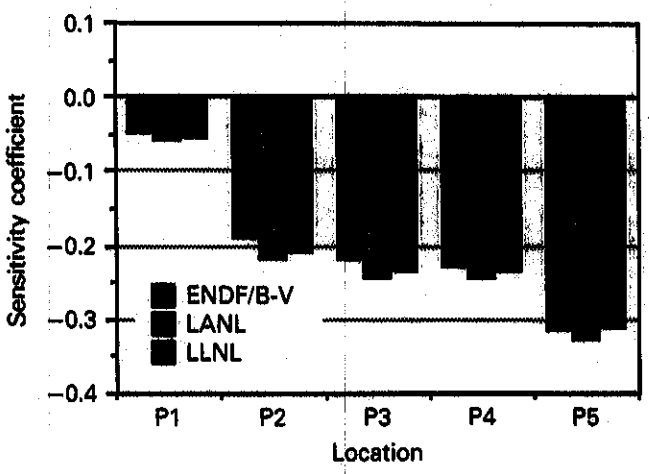

Fig. 20. Integrated sensitivity coefficient for T_7 due to a 1% increase in the total cross section of beryllium.

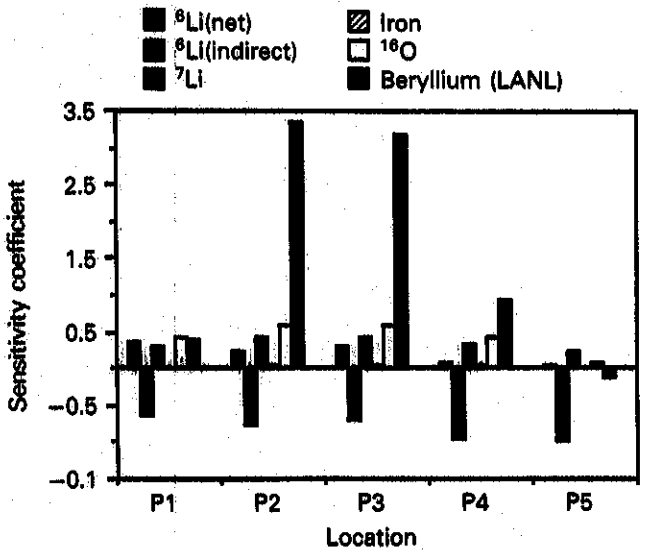

Fig. 21. Integrated sensitivity coefficient for T_6 due to a 1% increase in the total cross section of various materials.

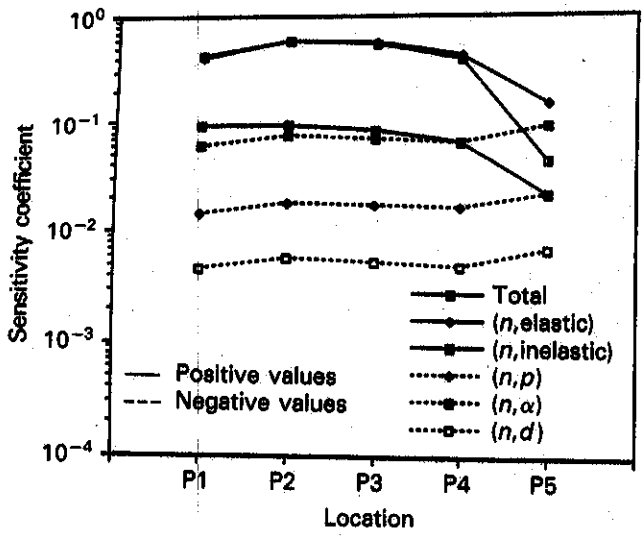

Fig. 22. Integrated relative sensitivity coefficient for T_6 due to variations in various partial cross sections of ^{16}O.

where it is clear that the largest contributions are from the $^{16}O(n,\text{elastic})$ cross section followed by the $^{16}O(n,\text{inelastic})$ cross section whose coefficients are positive at all locations. Note that the contribution from the $^{16}O(n,\alpha)$ cross section is relatively large, particularly at deep locations. Thus, by increasing the elastic and inelastic cross sections and by decreasing the (n,α) cross section, the T_6 profiles just behind the beryllium layer will increase; this leads to an improvement in the C/E curves shown in Fig. 6.

The coefficients for a 1% increase in the $^7Li(n,\text{total})$ cross section are always positive at all locations and are due to the increase in the $(n,2n)$, $(n,\text{elastic})$, $(n,n'\alpha)t$, and $(n,3n\alpha)$ cross sections, whose reactions lead to low-energy neutrons. Note that at deep locations (location P5), the relatively large coefficients are due to variations (increase) in the ^7Li cross sections. The *net* sensitivity coefficient due to a 1% increase in the $^6Li(n,\text{total})$ cross section is relatively small (except at location P1). Variations in the cross sections of other elements (iron, nickel, chromium, etc.) are noticeably smaller than those for the basic materials (beryllium, ^7Li, ^{16}O, ^6Li).

As for T_7, and aside from variation in the $^7Li(n,\text{total})$ cross section, the integrated sensitivity coefficients are all negative at all detector locations for variations in the total cross sections of other materials, as can be seen from Fig. 23. These coefficients get larger as one proceeds toward the back end of the Li_2O zone. The contribution from the variation in the σ_t of ^{16}O leads to the largest negative coefficients. The deeper the location of the detector is, the greater is the chance that neutrons are absorbed and do not contribute to T_7. Figure 24 shows the sensitivity coefficients for T_7 due to variations in the partial cross sections of ^{16}O at various detector locations. The dominant contribution comes from the $(n,\text{inelastic})$ cross section. The elastic cross section has positive coefficients, in contrast to all the other cross sections. As for variations in the σ_t of ^7Li, the direct part of the sensitivity profile, which is always positive, dominates the negative indirect contribution, which increases with depth. Variation in the σ_t of ^7Li has the most significant effect on the T_7 inside and around beryllium layer, while variation in the

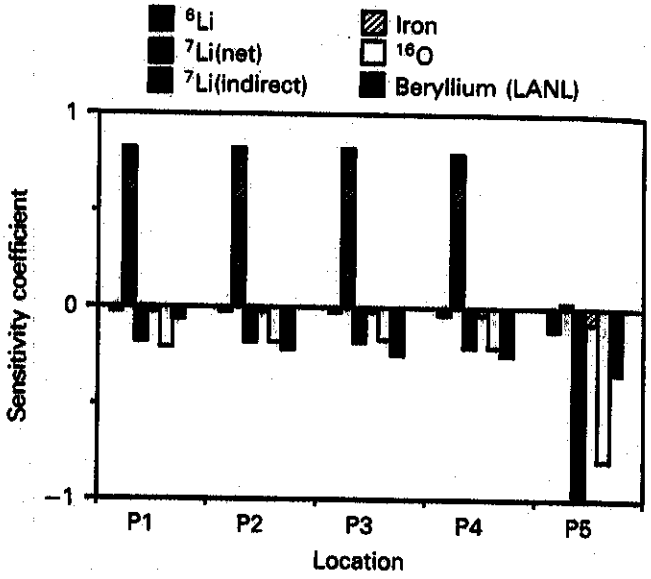

Fig. 23. Integrated sensitivity coefficient for T_7 due to a 1% increase in the total cross sections of various materials.

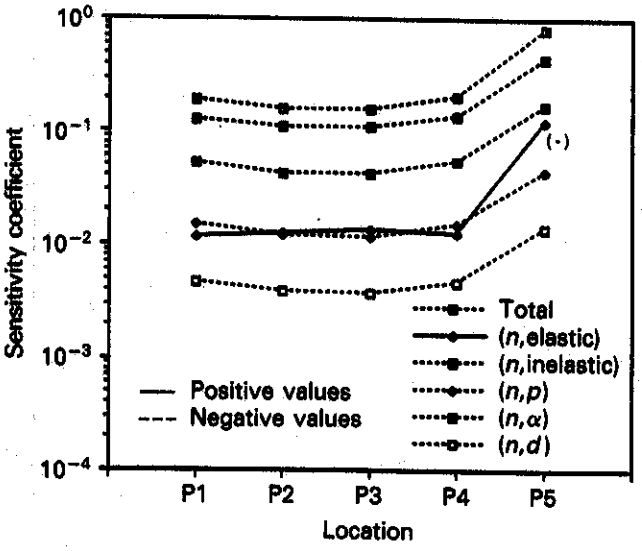

Fig. 24. Integrated relative sensitivity coefficients for T_7 due to variations in various partial cross sections of ^{16}O.

σ_t of beryllium leads to coefficients that are comparable to those of ^{16}O (this is in contrast to T_6 where the variation in the σ_t of beryllium has the largest coefficients at these locations).

From these results, the following can be stated regarding improvement in cross sections that lead to improved C/E values for T_6 and T_7. Just behind the beryllium layer, the underestimation of T_6 can be improved by increasing the $^9Be(n,elastic)$, $^9Be(n,2n)$, $^{16}O(n,elastic)$, and $^{16}O(n,inelastic)$ cross sections and decreasing the $^{16}O(n,\alpha)$ cross section. A 1% variation in that direction leads to integrated coefficients of 0.8, 0.25, 0.5, 0.08, and 0.08%, respectively, i.e., a net coefficient of ~1.7%. At deeper locations, these coefficients are −0.3, 0.2, 0.2, 0.02, and 0.1%, respectively, i.e., a net coefficient of ~0.22%. Thus, while improvement in the C/E values (increase) occurs just behind the beryllium layer, a further overestimation (but to a lesser extent) takes place at the bulk of the Li_2O zone. For T_7, this 1% variation leads to coefficients of −0.03, −0.2, 0.02, −0.15, and 0.05%, i.e., a net coefficient of −0.31% just behind the beryllium layer. These coefficients are −0.08, −0.22, 0.1, −0.5, and 0.1% at the deep locations, i.e., a net coefficient of −0.6%. Thus, in both cases, the overestimation in T_7 (shown in Fig. 6) is lessened.

V.B. Uncertainty Analysis Results

V.B.1. Results Due to Uncertainties in the Smooth Cross Sections of Materials

V.B.1.a. Uncertainty in T_6

The total RSDs in T_6 and T_7 due to uncertainties in the smooth cross sections of all materials are shown in Fig. 25. The RSDs in T_6 are 2.1, 9.3, 9.0, 3.2, and 2.5% for detector locations P1 through P5. More than 90% of the RSD in T_6 inside the beryllium layer is attributed to the uncertainties in the smooth cross sections of beryllium, while their contribution just behind the beryllium layer is ~80%. The contribution to the RSD in T_6 from each material is shown in Fig. 26. As shown, the contribution from the uncertainties in the ^9Be cross sections is the largest at all detector locations. This contribution is dominated by the uncertainties in the $^9Be(n,elastic)$ cross section inside and behind the beryllium layer. This is due to the large sensitivity coefficients of the $^9Be(n,elastic)$ cross section at these locations, as shown in Fig. 18. At deeper locations (location P5), the contribution from the uncertainties in the $^9Be(n,2n)$ cross section dominates that from the $^9Be(n,elastic)$ cross section (not shown). Note that the sensitivity coefficients of T_6 at these deep locations are positive for the $^9Be(n,2n)$ cross section but negative (and larger in absolute value) for the $^9Be(n,elastic)$ cross section, and the net coefficients are negative (see Figs. 17 and 18). The larger contribution to the RSD in T_6 that is attributed to the uncertainties in the $^9Be(n,2n)$ cross section at these deep locations indicate, therefore, that these uncertainties are larger than those for the $^9Be(n,elastic)$ cross section whose sensitivity coefficients are larger.

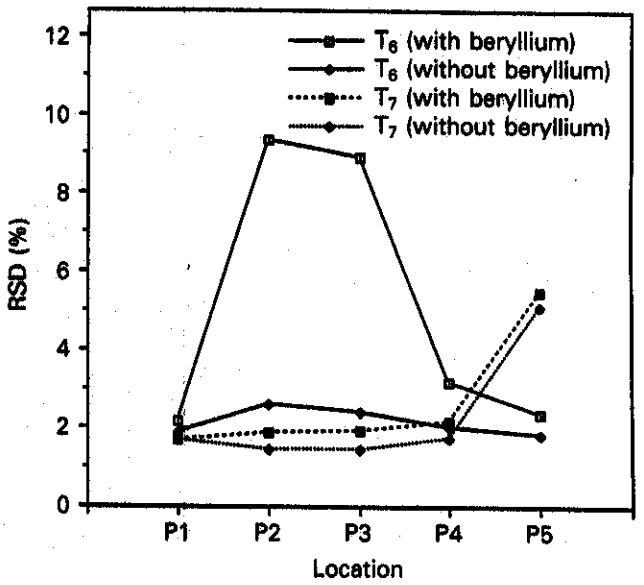

Fig. 25. Total RSD in T_6 and T_7 due to uncertainties in the cross sections of various materials.

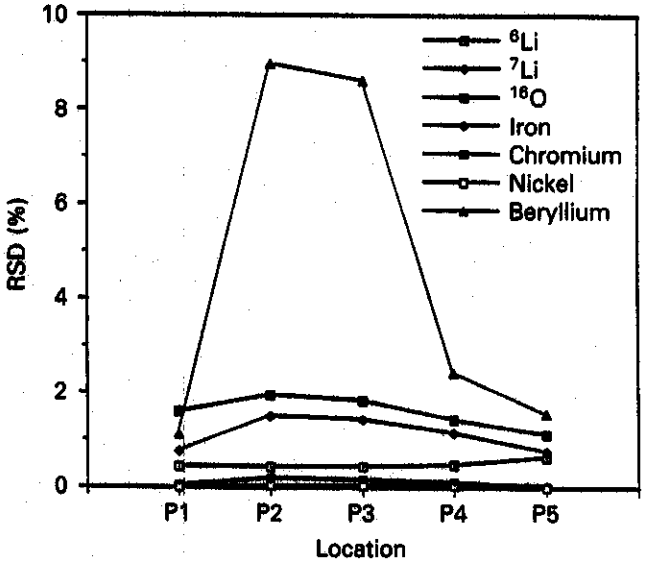

Fig. 26. The RSD in T_6 due to uncertainties in the cross sections of various materials. Point detectors are considered.

The RSD in T_6 due to uncertainties in the ^{16}O cross sections is the second largest contributor to the total RSD in T_6. This is due to the large values of the (positive) sensitivity coefficients for $^{16}O(n,elastic)$ and $^{16}O(n,inelastic)$ cross sections (see Fig. 22). The RSD in T_6 due to uncertainties in the ^7Li cross sections are

always larger than those due to uncertainties in the ^{6}Li data. This can be understood by examining the integrated relative sensitivity coefficients shown in Fig. 21, where these coefficients for ^{7}Li are larger than those for ^{6}Li. Also, the ratio of the RSD in T_6 due to the uncertainties in ^{7}Li cross sections to the RSD in T_6 due to uncertainties in the ^{16}O cross sections is almost the same as the ratio of their relative sensitivity coefficients shown in Fig. 21. The RSDs in T_6 due to uncertainties in the cross sections of other materials are always small compared with the principal elements (^{9}Be, ^{16}O, ^{7}Li, and ^{6}Li) at all detector locations. At deeper locations, all the RSDs in T_6 show smaller values than those at middle locations. If the contribution from the uncertainties in the beryllium cross sections is excluded, the RSD in T_6 is ~2.5%. This is consistent with the results of Ikeda and Youssef[50] for the reference experiment they analyzed in a two-dimensional model where no beryllium was utilized. Additionally, the largest RSDs in T_6 are observed in and behind the beryllium layer.

V.B.1.b. Uncertainty in T_7

The contributions to the RSD in T_7 arising from uncertainties in the cross sections of various materials are shown in Fig. 27. Uncertainties in the ^{16}O cross sections give the largest RSDs in T_7 at all detector locations (1.5% at P1 through P4 and 4.7% at P5). Generally, the RSD in T_7 increases as the detector location moves toward the back of the assembly, a trend that is consistent with the absolute values in the integrated relative sensitivity coefficients shown in Fig. 23.

The RSD in T_7 due to uncertainties in the ^{9}Be cross sections has an increasing trend similar to that observed in the case of ^{16}O. The RSDs of 1.2% in and around the beryllium layer and ~2% at deep locations are mostly attributed to the ^{9}Be(n,2n) cross section, whose sensitivity coefficients are large.

The total RSD in T_7 due to the uncertainties in the data of all the materials considered varies from 1.8 to 5.5%, as shown in Fig. 25. The contribution from the uncertainties in the cross sections of ^{16}O and ^{9}Be amounts to ~95% of the total RSD in T_7 at all detector locations. In particular, the contribution from the uncertainties in the ^{16}O cross section is ~75% at the back of the Li_2O assembly (detector location P5). Again, if the contribution from the uncertainties in the beryllium cross sections is excluded, the RSD in T_7 is ~1.8 to 5%, which is consistent with the results cited in Ref. 50. As for other materials, the RSDs in T_7 due to the uncertainties in their cross sections are small compared with those for the principal materials.

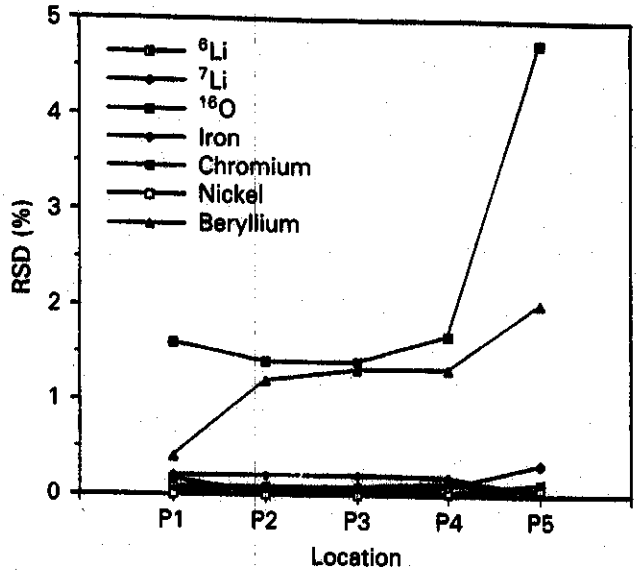

Fig. 27. The RSD in T_7 due to uncertainties in the cross sections of various materials. Point detectors are considered.

V.B.2. Results Due to Uncertainties in the SED of the ^{9}Be(n,2n) Cross Section

Generally, the relative variance of a response R can be obtained from

$$RVAR(R) = \sum_{g} \sum_{g'g''} P_{\Sigma_{gg'}} RCOV(\Sigma_{gg'}, \Sigma_{gg''}) P_{\Sigma_{gg''}} , \quad (27)$$

where

$RCOV(\Sigma_{gg'}, \Sigma_{gg''})$ = relative covariance matrix for the differential cross section of $\Sigma_{gg'}$

$P_{\Sigma_{gg'}}$ = SED sensitivity coefficient

g, g' = indices for incident and exit energy groups.

Currently, neither a covariance data file for the SED/SAD nor standard procedures (codes) are available to process such information. In principle, one can drive these uncertainties and covariance information by carefully examining the uncertainties in available measured data on the SED and SAD at several neutron incident energies and incorporating the driven covariance information (in multigroup form) in the manner shown in Eq. (27). However, the approach followed in this paper is to utilize the differences among readily available processed multigroup cross sections $\sigma_{gg'}$ of several evaluations as a basis for approximate uncertainties information. In this regard, if N independent evaluated data are available, the values for the variance of SED, $VAR(f_{gg'})$, can be roughly estimated for each SED as follows:

$$VAR(f_{gg'}) = \frac{1}{N-1} \sum_{j=1}^{N} (f_{gg'j} - \bar{f}_{gg'})^2 , \quad (28)$$

where

N = number of evaluated data set available

$f_{gg'} = \Sigma_{gg'}/\Sigma_g$ = normalized probability distribution in SED

$\bar{f}_{gg'} = \frac{1}{N}\sum_{j=1}^{N}(f_{gg'}j)$ = average value of the N number of data.

The RSD for evaluation j can be obtained from

$$\mathrm{RSD}(f_{gg'}j) = \frac{[VAR(f_{gg'})]^{1/2}}{f_{gg'}j} . \quad (29)$$

For our beryllium SED/SAD analysis, the three evaluations for the ^{9}Be(n,2n) cross section were used to derive the RSD for each element of the scattering matrix according to Eqs. (28) and (29). The relative variance of response R for an incident group g is obtained from the relative covariance matrix $RCOV(f_{gg'}, f_{gg''})$ as follows:

$$RVAR(R)_g = \sum_{g'g''} P_{gg'}(\mathrm{SED/SAD}) \cdot RCOV(f_{gg'}, f_{gg''}) \times P_{gg''}(\mathrm{SED/SAD}) , \quad (30)$$

where $P_{gg'}$ (SED/SAD) is the SED/SAD sensitivity coefficient. Since there is little knowledge of the energy correlation of SED/SAD uncertainties, correlation between different exit energy groups, g' and g'', can be assumed only as a full correlation or as an anticorrelation by comparing each element $f_{gg'}$ to the average distribution $\bar{f}_{gg'}$ as follows:

$$CORR(f_{gg'}, f_{gg''}) = \begin{cases} 1 , & \text{when } (f_{gg'} - \bar{f}_{gg'})(f_{gg''} - \bar{f}_{gg''}) > 0 \\ -1 , & \text{when } (f_{gg'} - \bar{f}_{gg'})(f_{gg''} - \bar{f}_{gg''}) < 0 . \end{cases}$$

One can argue that the uncertainty in the response under consideration could be estimated by simply calculating that response with each of the available evaluation for beryllium cross sections and then estimating the standard variation in the response from the several computed results. While this is true, the uncertainty in the response computed through this exercise is a combined estimate that does not distinguish the separate contributions from the uncertainties in the SED and the SAD. On the other hand, by considering the standard deviation in the normalized probability distribution $f_{gg'}$, one can incorporate this uncertainty information in the manner given by Eq. (30) to arrive at the uncertainty in the design parameter R. Nevertheless, there is an urgent need to have a more comprehensive covariance evaluation for the SED and SAD for beryllium cross sections that could, in principle, be processed into the formalism outlined in this paper.

The procedures described in Eqs. (27) through (30) were followed to derive the RSDs in the SED for the ^{9}Be(n,2n) cross section in each of the beryllium evaluations. Figures 28, 29, and 30 show these RSDs in the $\sigma_{gg'}$ elements of the ^{9}Be(n,2n) cross section for the ENDF/B-V, LANL, and LLNL evaluations, respectively. Note that the RSDs could be as large as 1000% (i.e., there is about an order of magnitude divergence among the three evaluations in some secondary energy ranges, which could lead to large uncertainties in T_6 and T_7). In the following, uncertainty analysis results due to uncertainties in the SED based on the LANL evaluation are given although parallel analysis was conducted using the ENDF/B-V and LLNL evaluations.

V.B.2.a. Results from the Excitation Level Treatment

The RSDs in the SED of the ^{9}Be(n,2n) cross section of the LANL evaluation, shown in Fig. 29, are large in the self-scattering region and in the lower secondary neutron energies ($E_{out} < 0.1$ MeV). When the RSDs are coupled with the SED sensitivity coefficients according to Eq. (30), we obtain the RSDs in T_6 and T_7 shown in Fig. 31, where the level-independent treatment was followed in obtaining the sensitivity coefficients. As shown, the first level variation has the largest RSD in T_6 while the third level variation gives the smallest values. This is because more secondary neutrons are concentrated at high energies in the first level variation case (see Fig. 11) where the RSDs in the SED are large, while the SED in the third level variation case is more pronounced around 2 to 4 MeV where the RSDs in the SED are relatively small, as shown in Fig. 29. The RSDs in T_7 show smaller values than of T_6 although the sensitivity coefficients of T_7 are a factor of 7 to 10 larger than those of T_6, as shown in Figs. 10 and 12. The trend of the RSDs of T_7 is similar to the corresponding sensitivity coefficients shown in Fig. 12.

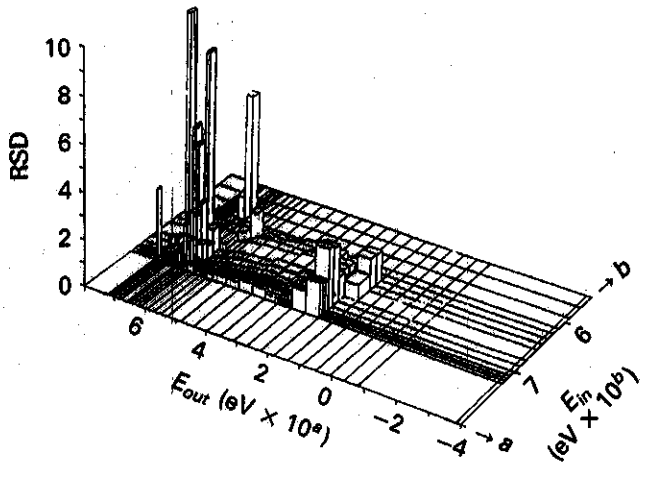

Fig. 28. The SED RSD in the ENDF/B-V ^{9}Be(n,2n) cross section: RSD of 1 means 100%.

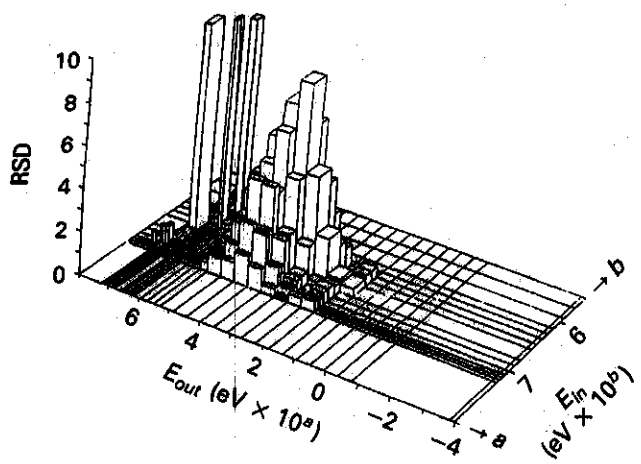

Fig. 29. The SED RSD in the LANL ^{9}Be(n,2n) cross section: RSD of 1 means 100%.

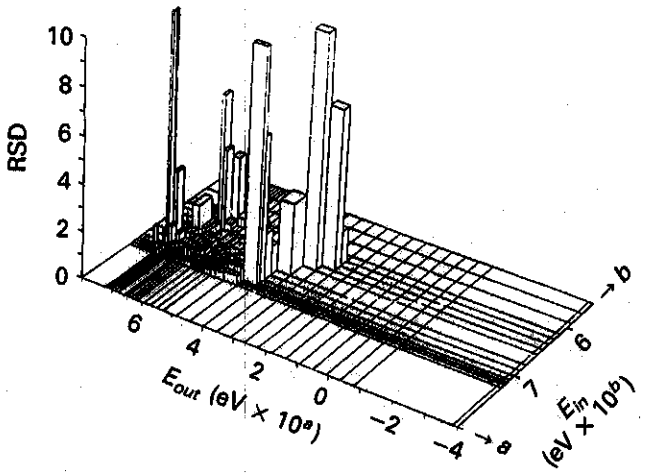

Fig. 30. The SED RSD in the ENDF/B-VI ^{9}Be(n,2n) cross section: RSD of 1 means 100%.

In the excitation level approach, the values of the RSDs in T_6 and T_7 with the LANL evaluation are larger than those obtained with the ENDF/B-V data for beryllium; this is attributed to the larger absolute values of the sensitivity coefficients for variations in the SED of the ^{9}Be(n,2n) cross sections as compared with the corresponding sensitivity coefficients obtained with the ENDF/B-V (and -VI) evaluations. In the level-dependent treatment, the same trends discussed earlier were observed (not shown).

V.B.2.b. Results from the Direct Variation in the SED

The two cases considered in this analysis are those discussed in Sec. V.A.1.b: case 1, a 1% decrease in the overestimated part of the SED ($0.5 < E_{out} < 10$ MeV) with a compensating increase in other energy ranges such that the total ^{9}Be(n,2n) cross section remains unchanged and case 2, a 1% increase in the SED of the lower energy part of the SED below 0.1 MeV with a compensating decrease in the SED above 0.1 MeV. The sensitivity coefficients obtained from these two cases were coupled with the RSDs of the SED in the manner discussed earlier for the three evaluations of beryllium.

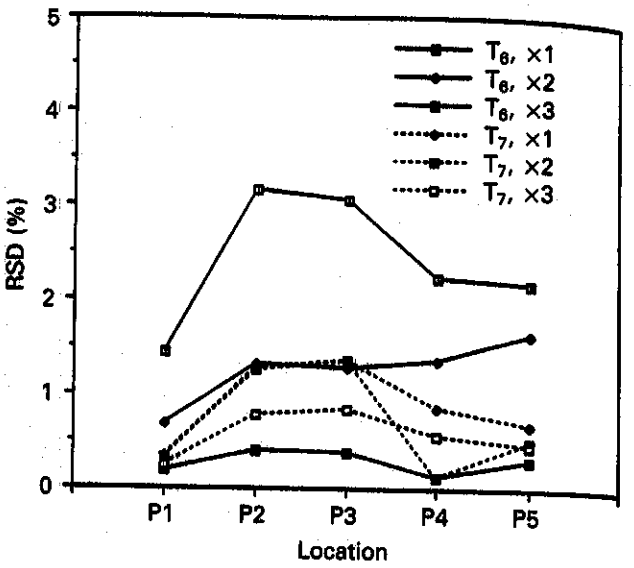

Fig. 31. The RSD in T_6 and T_7 due to uncertainties in the SED of the LANL ^{9}Be(n,2n) cross section (level-independent treatment).

As expected from the results of the sensitivity analysis, the large sensitivity coefficients in case 1 led to large RSDs in T_6 and T_7. The values of the RSDs in T_6 are as large as 11% inside beryllium and 9.5% behind the beryllium layer, as shown in Fig. 32. The results shown are based on the LANL evaluation. Note that the RSD in T_6 at the back location (P5) is relatively large although the sensitivity coefficients in case 1 are smaller at this location than inside and around the beryllium layer (see Fig. 13). This is due to the large RSDs in the SED at lower secondary neutron energies (E_{out} < 0.1 MeV), as shown in Fig. 29. The RSDs in T_7 also have large values (5% inside and 3 to 4% around the beryllium layer) compared with those obtained in the excitation level approach. In case 2, the RSDs in T_6 and T_7 are <0.5% because of the very small sensitivity coefficients, shown in Fig. 13.

V.B.3. Results Due to Uncertainties in the SAD of the ^{9}Be(n,2n) Cross Section

The RSDs in the first- and second-order Legendre polynomial transport scattering cross sections, $\sigma^1_{gg'}$ and $\sigma^2_{gg'}$, were calculated from the three available ^{9}Be(n,2n)

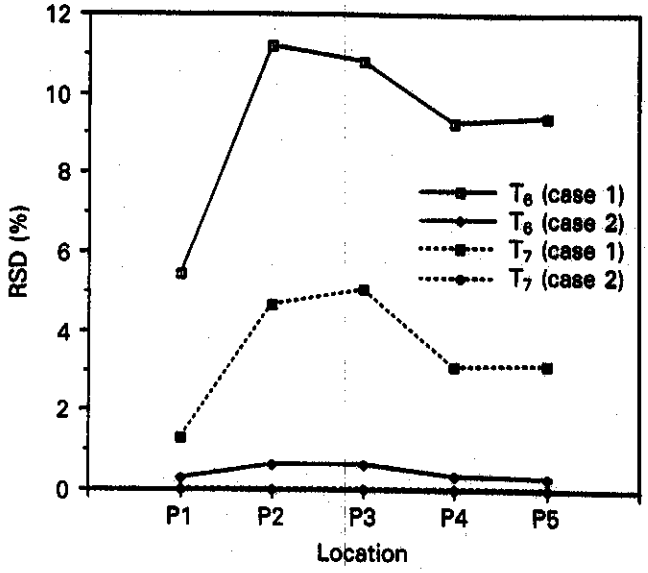

Fig. 32. The RSD in T_6 and T_7 due to uncertainties in the SED of the LANL $^9Be(n,2n)$ cross section (direct variation).

multigroup cross-section libraries. The RSDs in the first-order transport scattering cross section $\sigma^1_{gg'}$ were used in the forward and backward variations, and the RSDs in the second-order transport scattering cross section $\sigma^2_{gg'}$ were used in the upward variation, as outlined in Sec. IV.B.2. These RSDs were coupled with the SAD sensitivity coefficients according to Eq. (30) to obtain the RSDs in T_6 and T_7.

Figure 33 shows the RSDs in T_6 and T_7 due to uncertainties in the SAD of the LANL $^9Be(n,2n)$ cross section. Similar results were obtained with the ENDF/B-V and LLNL evaluations. The RSDs in T_6 and T_7 with the three evaluations are small (less than ~1%) except at the back locations in the forward and backward variations, especially for T_6. This trend is consistent with the corresponding absolute values of the integrated relative sensitivity coefficients shown, for example, in Figs. 15 and 16. Note that the RSD in T_6 at detector location P4 (just behind the beryllium layer) is ~1% in both the forward and backward variations in the ENDF/B-V (not shown) and LANL evaluations and 0.35% in the case of the LLNL evaluation (not shown). The RSDs in T_6 inside the beryllium layer are <1% (0.3% in the ENDF/B-V and LANL cases and 0.2% in the LLNL case). The RSDs in T_7 are generally smaller than those for T_6, and for both responses, the RSDs are an order of magnitude lower than those obtained in the case of variations in the SED.

V.B.4. Summary of Uncertainty Analysis Results

Table II shows the RSDs in T_6 and T_7 that result from uncertainties in the smooth integrated cross sections and uncertainties in the SED and SAD of the $^9Be(n,2n)$ cross section. Although the results discussed in this paper focus on the LANL evaluation for beryllium, Table II gives results from parallel analyses using the ENDF/B-V and LLNL evaluations. For example, the results cited in Table II for the effect of the uncertainty in the $^9Be(n,2n)$ cross section of ENDF/B-V on T_6 and T_7 involved coupling the SED sensitivity coefficients for variation in the second excitation level (χ_2, E_{th} = 2.43 MeV) as the prime level (this type of variation gives the largest sensitivity coefficients in both the level-dependent and the level-independent treatment) with the uncertainties in the SED shown in Fig. 28.

V.B.4.a. Discrepancy Between Calculations and Measurements for T_6

As shown in Table II, the uncertainties in T_6 due to uncertainties in the integrated cross-section data themselves are ~2.5% in the bulk of the Li_2O zone, ~3.2% just behind the beryllium layer, and ~9.3% inside the beryllium layer. As indicated earlier, these uncertainties are mainly due to uncertainties in the $^9Be(n,elastic)$ cross section, particularly inside the beryllium layer. The smaller contribution to the RSDs in T_6 is attributed to uncertainties in the oxygen data, particularly the $(n,elastic)$, $(n,inelastic)$, and (n,α) cross sections. These uncertainties and the uncertainties in the ^7Li data contribute appreciably to the RSDs in T_6 in the bulk of the Li_2O zone (see Fig. 26). The impact of the uncertainties in the SED of the $^9Be(n,2n)$ cross section is not negligible, particularly if direct variation in the SED of the LANL $^9Be(n,2n)$ evaluation is considered. Inside the beryllium layer, these uncertainties lead to ~11.2% RSDs in T_6 (excitation level treatment

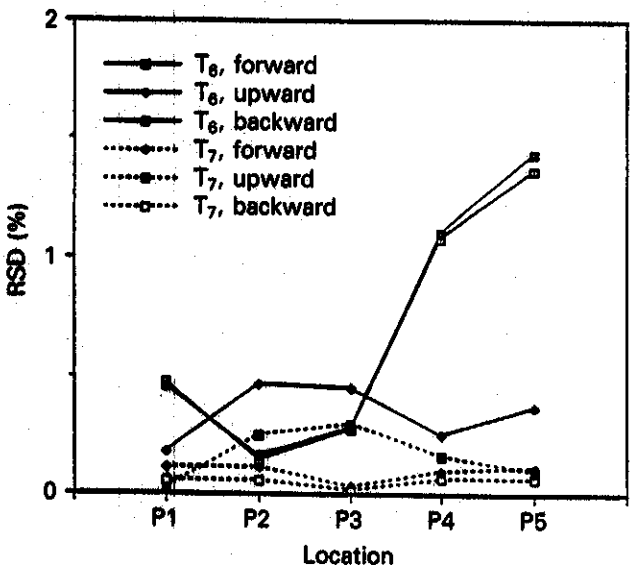

Fig. 33. The RSD in T_6 and T_7 due to uncertainties in the SAD of the LANL $^9Be(n,2n)$ cross section.

TABLE II

Relative Standard Deviations in T_6 and T_7 Due to Uncertainties in Nuclear Data, Including Uncertainties in the SED and SAD of the $^9Be(n,2n)$ Cross Section

Detector Location	Cross Section[a] (%)	SED[b] (%)			SAD[b] (%)		
		ENDF/B-V (X_2)[c]	LANL (X_1)[c]	LANL Direct Variation	ENDF/B-V (Forward)	LANL (Forward)	LLNL (Forward)
T_6							
P_1	2.1	1.0 (2.33)[d]	1.4 (2.5)[d]	5.2 (5.6)[d]	0.122 (2.1)[d]	0.47 (2.2)[d]	0.05 (2.1)[d]
P_2	9.3	1.65 (9.45)	3.2 (9.8)	11.2 (14.6)	0.25 (9.3)	0.14 (9.3)	0.12 (9.3)
P_3	9.0	1.6 (9.1)	3.1 (9.5)	11 (14.2)	0.29 (9.0)	0.27 (9.0)	0.12 (9.0)
P_4	3.2	1.8 (3.7)	2.3 (3.9)	9.2 (9.7)	0.9 (3.3)	1.08 (3.4)	0.71 (3.3)
P_5	2.5	2.1 (3.3)	2.2 (3.3)	9.3 (9.6)	1.83 (3.1)	1.37 (2.9)	0.59 (2.6)
T_7							
P_1	1.8	0.3 (1.8)	0.3 (1.8)	1.2 (2.2)	0.26 (1.8)	0.11 (1.8)	0.05 (1.8)
P_2	1.9	0.55 (2.0)	1.25 (2.3)	4.6 (5.0)	0.26 (1.9)	0.11 (1.9)	0.05 (1.9)
P_3	1.95	0.57 (2.1)	1.3 (2.3)	4.9 (5.3)	0.075 (1.95)	0.035 (1.95)	0.015 (1.9)
P_4	2.05	0.2 (2.1)	1.0 (2.3)	3.1 (3.7)	0.12 (2.05)	0.1 (2.05)	0.02 (2.05)
P_5	5.5	0.1 (5.5)	0.8 (5.6)	3.2 (6.4)	0.21 (5.5)	0.11 (5.5)	0.105 (5.5)

[a]Uncertainties in the cross section.
[b]Uncertainties in the SED and SAD.
[c]Variation of the n'th excitation level in the ENDF/B-V and LANL evaluations.
[d]Square root of $a^2 + b^2$; total uncertainties when uncertainties in the SED and SAD are included.

leads to 2 to 3% RSDs in T_6). In the bulk of the breeding zone, the RSD in T_6 is ~9.3% due to uncertainties in the SED. Even with the excitation level treatment, the resultant uncertainties in T_6 in the breeding zone is comparable (~2%) to those obtained from the current uncertainties in the integrated cross sections (~2.5%). The uncertainties in T_6 inside the beryllium layer due to uncertainties in the SAD of the $^9Be(n,2n)$ cross section are smaller (<0.3%) than those attributed to the uncertainties in the SED of this reaction. When the largest numbers from Table II are used, the combined uncertainties in T_6 inside the beryllium layer, just behind it, and at the bulk of the Li_2O zone are ~14.6, ~9.9, and ~9.8%, respectively, where the largest effect from the uncertainties in the SED and SAD of the $^9Be(n,2n)$ cross section is considered. Thus, the large discrepancy (C/E ~ 1.4 with the LANL and LLNL evaluations) between calculations and measurements inside the beryllium layer (see Fig. 6) cannot be explained only by the uncertainties in nuclear data. The self-shielding effect is the main source for this discrepancy. Flux depression occurs in the finite-size detectors used to measure T_6, and the apparent measured values are therefore smaller than the calculated ones. It was shown[51] that if the calculational model accounts for the geometrical details of the detectors and the associated detection system, the contribution to the discrepancy that is attributed to the self-shielding effect is ~30%, while the contribution due to flux perturbation by the detector and the associated components is ~20%. Therefore, in our analysis, the uncertainty in the nuclear data contributes about ±15% in addition to these sources of discrepancy inside the beryllium layer. The C/E values just behind the beryllium layer are ~0.9 (with ENDF/B-V) and ~0.95 (with the LANL and LLNL evaluations), as can be seen in Fig. 6. The contribution (2 to 3%) to this discrepancy that comes from uncertainties in the smooth cross sections cannot cover the ~10% discrepancy obtained with the LANL or LLNL data for beryllium. The RSD in T_6 of 9.7% due to uncertainties in the SED of the $^9Be(n,2n)$ reaction can partly cover the observed 10% discrepancy just behind the beryllium layer, but other sources lead to this discrepancy. Among these sources are the following:

1. *The interpolation scheme applied:* The T_6 profile is very steep at the boundaries between the beryllium layer and the adjacent Li_2O zone because of the sudden change in the neutron spectrum inside and outside this layer. Therefore, the calculated values are very sensitive to the interpolation scheme applied to calculate those values at the exact measuring locations. Our analysis indicates that a 4 to 6% difference in the C/E values could arise from the different interpolation schemes applied (log-linear, log-log, and Lagrangian) at the Be/Li_2O boundaries. However, no apparent differences occurred in the C/E values evaluated with these interpolation schemes at locations farther away ($z > 15$ cm) from the beryllium layer and inside the Li_2O zone.

2. *Error in the exact measuring locations:* When the calculated values are interpolated at locations shifted 0.1 cm from the original locations of the measuring points (i.e., $z_{new} = z \pm 0.1$ cm), the C/E values behind the beryllium layer are greatly changed. This particular variation assumes that the exact measuring locations could be in error by ~0.1 cm. A 0.1-cm error in defining the exact measuring locations could lead to a 15% decrease in the C/E values at a distance of $z = 1.4 + 0.1$ cm and an ~2% increase at $z = 1.4 - 0.1$ cm behind that layer.

3. *Size of mesh intervals in the calculational model:* As mentioned earlier, the T_6 profile is very steep at the Be/Li_2O boundaries; therefore, the calculated values could have large uncertainties depending on the size of the mesh intervals applied in the transport calculations. To investigate this effect, smaller mesh intervals were applied behind the beryllium layer ($\Delta z = 0.1$ cm), and the results were compared with those obtained with a relatively larger mesh size ($\Delta z = 0.64$ cm). It was found that the C/E values differ by ~2% between these two cases.

It can be said from the above that differences in the interpolation scheme applied, errors in the exact measuring locations, and the size of the spatial mesh used just behind the beryllium layer lead to ~4 to 6, ~2 to 15, and ~2% differences, respectively, in the calculation of T_6. By considering the additional 9.6% uncertainty in T_6 due to data uncertainty, the observed discrepancy of ~10% behind the beryllium layer can be explained. In the bulk of the Li_2O zone, the observed overestimation of ~10% in T_6 could be covered by the RSD in T_6 (~9.6%) due to data uncertainties, provided the contribution from the SED uncertainties in the $^9Be(n,2n)$ reaction is considered.

V.B.4.b. Discrepancy Between Calculations and Measurements for T_7

The uncertainties in T_7 due to uncertainties in the integrated cross-section data are ~5.5% in the bulk of the Li_2O zone, ~2% just behind the beryllium layer, and ~2% inside the beryllium layer. The largest uncertainties occurred at the back locations in the Li_2O assembly. These uncertainties are mainly due to the current uncertainties in the $^{16}O(n,\text{inelastic})$, $^{16}O(n,\alpha)$, $^{16}O(n,p)$, and $^9Be(n,2n)$ cross sections, and the uncertainties in oxygen data are the main contributor to the RSDs in T_7, especially at deep locations. Inside the beryllium layer, the uncertainties in the SED of the $^9Be(n,2n)$ cross section could lead to ~5% uncertainties in T_7 and ~3% behind the beryllium layer and in the bulk of the Li_2O zone. The contribution to the RSDs in T_7 attributed to the uncertainties in the SAD of the $^9Be(n,2n)$ reaction is negligible (~0.1%). Thus, the total RSDs in T_7 inside the beryllium layer, just behind it, and in the bulk of the assembly are ~5.3, ~3.7, and ~6.4%, respectively. Unlike T_6, both the uncertainties in T_7 and the C/E values do not change noticeably between locations inside and outside the beryllium layer. As shown in Fig. 6, the C/E value for T_7 inside the beryllium layer is ~1.13 (with the LANL and LLNL evaluations for beryllium) and ~2 to 20% in the bulk of the Li_2O zone. Note from Fig. 6 that T_7 obtained by the LLNL evaluation is the largest because of the smaller $^9Be(n,2n)$ cross section in this evaluation as compared with LANL or ENDF/B-V. Increasing the $^9Be(n,2n)$ cross section in the LLNL evaluation will improve the C/E values for T_7. The 5 to 6% RSDs in T_7 due to the combined (total) uncertainties in data (including SED and SAD) could partly cover the 2 to 20% discrepancy between the calculations and measurements in the bulk of the Li_2O zone, but not inside the beryllium layer. Note that the experimental values for T_7 were obtained by the NE-213 indirect method in which the measured spectrum is folded with the $^7Li(n,n'\alpha)t$ cross section of JENDL3-PR1 (Ref. 52). It was shown that this cross section is underestimated by 8 to 10% at high incident energies, which consequently leads to lower experimental values (larger C/E values) with the NE-213 indirect method. This could partly explain the 2 to 20% overestimation in T_7 in the bulk of the Li_2O zone.

VI. CONCLUSIONS

A new approach for treating the sensitivity and uncertainty in the secondary neutron energy distribution and secondary neutron angular distribution was developed, and the algorithm was incorporated into the two-dimensional cross-section sensitivity and uncertainty analysis code, FORSS. This new approach was applied to examine the effect of the current uncertainties in the SED and SAD of the $^9Be(n,2n)$ cross section on the TPR from ^6Li (T_6) and ^7Li (T_7) in an engineering-oriented fusion integral experiment where beryllium was used as a neutron multiplier. The new approach is based on varying the contribution of a particular excitation level of the many levels used to describe the $^9Be(n,2n)$ cross section to the total SED with a compensating alteration in the contributions of other levels such that the total integrated $^9Be(n,2n)$ cross section remains the same. Direct variations in the total SED and SAD were also examined to derive the relative sensitivity profiles for variations in the SED as well as the SAD. The variations applied are arbitrary but can be performed to conform with observations on the SED obtained from experimental results. The sensitivity profiles were then coupled with the uncertainties in the SED and SAD of the $^9Be(n,2n)$ cross section. To date, there is a lack of information on the covariance data for these distributions. To pursue the analysis, therefore, it was necessary to derive approximate RSDs in elements of the multigroup transfer matrix $\sigma_{gg'}$ for the

^{9}Be(n,2n) cross section based on comparisons made among three evaluations for beryllium data, namely, the ENDF/B-V, LANL, and LLNL (ENDF/B-VI) evaluations. The SED of the ^{9}Be(n,2n) cross section differs appreciably in these three evaluations, and in some cases, the RSD in $\sigma_{gg'}$ could be as large as 1000%. Although the purpose of this analysis is not to examine the accuracies of these evaluations, these evaluations were used as bases to derive the RSDs in the SED (and SAD) of the ^{9}Be(n,2n) cross section that are required for the uncertainty analysis.

A comprehensive two-dimensional sensitivity/uncertainty analysis was performed on the smooth integrated cross sections of beryllium and other materials as well as the SED and SAD to arrive at an estimate for the uncertainties in the predictions of T_6 and T_7 that are attributed to nuclear data uncertainties. The analysis was performed to investigate the reasons for the discrepancies between calculated and measured values for local T_6 and T_7 at several locations in the test assembly of the beryllium-sandwiched experiment of phase IIA of the DOE/JAERI Collaborative Program on Fusion Neutronics. Without considering the uncertainties in the SED and SAD of the ^{9}Be(n,2n) cross section, the uncertainties in T_6 were ~2 to 3% in the Li_2O zone, whereas they are ~10% when the uncertainties in the SED and SAD of the ^{9}Be(n,2n) cross section are accounted for. Inside the beryllium layer, these uncertainties are ~15 and ~9% with and without results from the SED and SAD analysis. The contribution from the SAD uncertainties is small in this case (~1%). As for T_7, the uncertainties in the Li_2O zone with and without considering the SED and SAD results are 4 to 7 and 2 to 5.5%, respectively. The estimated uncertainties in T_6 and T_7 could partly explain the discrepancies between the calculations and measurements, although other sources for these discrepancies have been identified. The results obtained in this study demonstrate the importance of including the uncertainties in the SED and SAD in any cross-section sensitivity/uncertainty analysis, particularly for those reactions that affect the responses under consideration such as the ^{9}Be(n,2n) reactions. However, there is an immediate need to generate covariance data for these distributions in the evaluated nuclear data files to conduct more accurate cross-section sensitivity/uncertainty analyses.

ACKNOWLEDGMENT

This work was performed under the DOE grant DE-FG03-86ER52124.

REFERENCES

1. M. A. ABDOU et al., "A Blanket Comparison and Selection Study—Interim Report," ANL/FPP/TM-177, Argonne National Laboratory (1983).

2. Bulk Interim Reports 2-11, COPE-2338, Lawrence Livermore National Laboratory (1955–1956).

3. P. CLOTH, D. FULGES, R. HERZING, and N. KIRCH, "Neutron Multiplication Effect of CTR Blankets Containing Beryllium," *Proc. 9th Symp. Fusion Technology*, Garmisch-Partenkirchen, Germany, June 14–18, 1976, p. 569, Pergamon Press (1976).

4. T. K. BASU, V. R. NARGUNDKAR, P. CLOTH, D. FULGES, and S. TACZANOWSKI, "Neutron Multiplication Studies in Beryllium for Fusion Reactor Blanket," *Nucl. Sci. Eng.*, **70**, 309 (1979).

5. V. R. NARGUNDKAR, T. K. BASU, O. P. JONEJA, M. R. PHISKE, and S. K. SADAVARTE, "Neutron Multiplication Measurement in BeO for 14-MeV Neutrons," *Fusion Technol.*, **6**, 93 (1984).

6. V. R. NARGUNDKAR, T. K. BASU, and O. P. JONEJA, "Reanalysis of Neutron Multiplication Measurements in Thick Beryllium and Graphite Assemblies for 14 MeV Neutrons," *Fusion Technol.*, **12**, 380 (1987).

7. C. WONG, E. F. PLECHATY, R. W. BAUER, R. C. HAIGHT, L. F. HANSON, R. J. HOWERTON, T. T. KOMOTO, J. D. LEE, S. T. PERKINS, and B. A. POHL, "Measurements and Calculations of the Leakage Multiplication from Hollow Beryllium Sphere," *Fusion Technol.*, **8**, 1165 (1985).

8. A. A. ANDROSENKO, P. A. ANDROSENKO, B. V. DEVKIN, B. V. ZHURAVLEV, M. G. KOBAZEV, O. A. SALNIKOV, S. P. SIMAKOV, V. A. ZAGRYADSKY, D. V. MARKOVSKIJ, and D. Yu. CHUVILIN, "Measurement and Comparison with Calculations of Neutron Leakage Spectra from U, Pb, Be Spheres with Central 14 MeV Neutron Source," *Proc. Specialists Mtg. Neutronics and Thermohydraulics of OTR Project*, Varna, Bulgaria, May 5–7, 1987.

9. B. E. LESHCHENKO, Yu. N. ONISHCHUK, A. B. MELNICHENKO, A. A. BORISOV, D. V. MARKOVSKIJ, and D. Yu. CHUVILIN, "Time-of-Flight Measurement of Neutron Leakage Spectrum from a Beryllium Sphere with a Central 14 MeV Neutron Source," IAE-5230/8, Kurchatov Institute of Atomic Energy (1990) (in Russian); presented at IAEA Advisory Group Mtg. Nuclear Data for Neutron Multiplication in Fusion Reactor First Wall and Blanket Materials, Chengdu, People's Republic of China, November 19–21, 1990.

10. H. EBI, W. EYRICH, H. FRIES, H. GIESE, K. HAYASHI, F. KAPPLER, U. VON MÖLLENDORFF, and T. TSUKIYAMA, "Measurement of Neutron Transport and Multiplication in Beryllium," presented at 2nd Int. Symp. Fusion Nuclear Technology, June 2–7, 1991, Karlsruhe, Germany; see also *Fusion Eng. Des.*, **18**, 317 (1991).

11. J. R. SMITH and J. J. KING, "Neutron Multiplication in Bulk Beryllium," *Fusion Technol.*, **19**, 1924 (1991).

12. Y. CHEN, G. CHEN, R. LIU, H. GUO, W. CHENN, W. JIAN, and J. SHEN, "Experiment of Neutron Multiplication in Beryllium," presented at IAEA Advisory Group Mtg. Nuclear Data for Neutron Multiplication in Fusion Reactor First Wall and Blanket Materials, Chengdu, People's Republic of China, November 19–21, 1990.

13. U. FISCHER, A. SCHWENK-FERRERO, and E. WIEGNER, "Analyses of 14 MeV Neutron Transport in Beryllium," presented at 2nd Int. Symp. Fusion Nuclear Technology, June 2–7, 1991, Karlsruhe, Germany; see also *Fusion Eng. Des.*, **18**, 361 (1991).

14. P. G. YOUNG and L. STEWART, "Evaluated Data for n + ^{9}Be Reactions," LA-7932-MS, Los Alamos National Laboratory (July 1979).

15. S. T. PERKINS, E. F. PLECHATY, and R. J. HOWERTON, "A Re-Evaluation of the ^{9}Be(n,2n) Reaction and Its Effect on Neutron Multiplication in Fusion Blanket Applications," *Nucl. Sci. Eng.*, **90**, 83 (1985).

16. J. W. DAVIDSON and M. E. BATTAT, "Calculation of the INEL Beryllium Multiplication Experiment," *Fusion Technol.*, **19**, 2006 (1991).

17. Y. OYAMA and H. MAEKAWA, "Measurement and Analysis of an Angular Neutron Flux on a Beryllium Slab Irradiated with Deuterium-Tritium Neutrons," *Nucl. Sci. Eng.*, **97**, 220 (1987).

18. U. FISCHER, A. SCHWENK-FERRERO, and E. WIEGNER, "Neutron Multiplication in Lead: A Comparative Study Based on a New Calculational Procedure and New Nuclear Data," *Proc. 1st Symp. Fusion Nuclear Technology*, Tokyo, Japan, April 10–19, 1988, Part C, p. 139 (1988).

19. A. SCHWENK-FERRERO, "Verfahren zur numerischen Lösung der Neutronentransportgleichung mit strenger Behandlung der anisotropen Streuung," KfK-4788, Kernforschungszentrum Karlsruhe (Sep. 1990).

20. M. Z. YOUSSEF, C. GUNG, M. NAKAGAWA, T. MORI, K. KOSAKO, and T. NAKAMURA, "Analysis and Intercomparison for Phase I Fusion Integral Experiments at the FNS Facility," *Fusion Technol.*, **10**, 549 (1986).

21. M. Z. YOUSSEF, M. A. ABDOU, C. GUNG, R. J. SANTORO, R. G. ALSMILLER, J. M. BARNES, T. A. GABRIEL, M. NAKAGAWA, T. MORI, K. KOSAKO, Y. IKEDA, and T. NAKAMURA, "Phase I Fusion Integral Experiments," Vol. II—Analysis, UCLA-ENG-88-15, University of California–Los Angeles (Sep. 1988); see also JAERI-M-88-177, Japan Atomic Energy Research Institute (Aug. 1988).

22. T. NAKAMURA and M. A. ABDOU, "Summary of Recent Results from the JAERI/US Fusion Neutronics Phase I Experiment," *Fusion Technol.*, **10**, 541 (1986).

23. Y. OYAMA, S. YAMAGUCHI, K. TSUDA, Y. IKEDA, C. KONNO, H. MAEKAWA, T. NAKAMURA, K. G. PORGES, E. F. BENNET, and R. F. MATTAS, "Phase IIB Experiments of the US/JAERI Collaborative Program on Fusion Neutronics," *Fusion Technol.*, **15**, 1293 (1989).

24. M. Z. YOUSSEF, Y. WATANABE, M. A. ABDOU, M. NAKAGAWA, T. MORI, K. KOSAKO, and T. NAKAMURA, "Comparative Analysis for Phase IIA and IIB Experiments of the US/JAERI Collaborative Program on Fusion Breeder Neutronics," *Fusion Technol.*, **15**, 1299 (1989); see also M. Z. YOUSSEF et al., "The US/JAERI Collaborative Program on Fusion Neutronics: Phase IIA and IIB Fusion Integral Experiments: The US Analysis," UCLA-ENG-90-14, FNT31, The University of California–Los Angeles (Dec. 1989).

25. M. NAKAGAWA, T. MORI, K. KOSAKO, Y. OYAMA, and T. NAKAMURA, "JAERI/US Collaborative Program on Fusion Blanket Neutronics, Analysis of Phase IIA and IIB Experiments," JAERI-M-89-154, Japan Atomic Energy Research Institute (Oct. 1989).

26. M. Z. YOUSSEF and Y. WATANABE, "Study on the Accuracy of Several Beryllium Data Evaluations and Comparison of Measured and Calculated Data on Reaction Rates and Tritium Production Distributions," *Fusion Technol.*, **19**, 1967 (1991).

27. D. M. DRAKE, G. F. AUCHAMPAUGH, E. D. ARTHUR, C. E. RAGAN, and P. G. YOUNG, "Double-Differential Beryllium Neutron Cross-Sections at Incident Neutron Energies of 5.9, 10.1, and 14.2 MeV," *Nucl. Sci. Eng.*, **63**, 401 (1977).

28. M. BABA et al., "The Interaction of Fast Neutrons with ^{9}Be," *Proc. Int. Conf. Neutron Physics and Nuclear Data*, Harwell, U.K., September 25–29, 1978, p. 198.

29. A. TAKAHASHI, E. ICHIMURA, Y. SASAKI, and H. SUGIMOTO, "Measurement of Double Differential Neutron Emission Cross Sections for Incident Neutrons of 14 MeV," *J. Nucl. Sci. Technol.*, **25**, 215 (1988).

30. R. A. MACFARLANE, D. W. MUIR, and R. M. BOICOURT, "The NJOY Nuclear Data Processing System," Vols. I and II (ENDF-9303-M); Vol. I, LA-9303-M; and Vol. II (ENDF-324), Los Alamos National Laboratory (May 1982).

31. R. A. MACFARLANE, "TRANSX-CTR: A Code for Interfacing MATXS Cross-Section, Libraries to Nuclear Transport Codes for Fusion Systems Analysis," LA-9863-MS, Los Alamos National Laboratory (Feb. 1984).

32. N. M. GREEN et al., "AMPX: Modular Code System for Generation Coupled Multigroup Neutron-Gamma Ray Cross-Section Library from Data in ENDF Format," PSR-063/AMPXII, ORNL/TM-3706, Radiation Shielding Information Center, Oak Ridge National Laboratory (1980).

33. S. YAMAGUCHI et al., "An On-Line Method for Tritium Production Measurement with a Pair of Lithium-Glass Scintillators," *Nucl. Instrum. Methods*, **A245**, 413 (1987).

34. S. A. GERSTL et al., "A Comprehensive Neutron Cross Section and Secondary Energy Distribution Uncertainty Analysis for a Fusion Reactor," LA-83333-MS, Los Alamos National Laboratory (May 1980).

35. M. EMBRECHT, "Two-Dimensional Cross-Section Sensitivity and Uncertainty Analysis for Fusion Reactor Blanket," LA-9232-T, Los Alamos National Laboratory (1982).

36. K. FURUTA, Y. OKA, and S. KONDO, "A Cross-Section Sensitivity and Uncertainty Analysis on Fusion Reactor Blankets with SAD/SED Effect," *Nucl. Eng. Des./Fusion*, **3**, 287 (1986).

37. M. Z. YOUSSEF, "Status of Methods, Codes and Applications for Sensitivity and Uncertainty Analysis," *Fusion Technol.*, **8**, 1552 (1985).

38. R. L. CHILDS, "Generalized Perturbation Theory Using Two-Dimensional, Discrete Ordinates Transport Theory," ORNL/CSD/TM-127, Oak Ridge National Laboratory (1980).

39. R. G. ALSMILLER, Jr., R. T. SANTORO, J. BARISH, and T. A. GABRIEL, "Comparison of the Cross-Section Sensitivity of the Tritium Breeding Ratio in Various Fusion-Reactor Blankets," *Nucl. Sci. Eng.*, **57**, 122 (1975).

40. D. E. BARTINE, R. G. ALSMILLER, Jr., E. M. OBLOW, and F. R. MYNATT, "Cross-Section Sensitivity of Breeding Ratio in a Fusion-Reactor Blanket," *Nucl. Sci. Eng.*, **53**, 304 (1974).

41. S. A. W. GERSTL, D. J. DUDZIAK, and D. W. MUIR, "Cross-Section Sensitivity and Uncertainty Analysis with Application to a Fusion Reactor," *Nucl. Sci. Eng.*, **62**, 137 (1977).

42. M. Z. YOUSSEF, R. W. CONN, and C. W. MAYNARD, "Impact of Cross-Section Uncertainties on the Nuclear Design of Hybrid Reactors," *Nucl. Technol./Fusion*, **2**, 648 (1982).

43. M. Z. YOUSSEF and M. A. ABDOU, "Uncertainties in Prediction of Tritium Breeding in Candidate Blanket Designs Due to Present Uncertainties in Nuclear Data Base," *Fusion Technol.*, **9**, 286 (1986).

44. "DLC-113/VITAMIN-E: A Coupled 174 Neutron, 28 Gamma Ray Multigroup Cross-Section Library for Deriving Application-Dependent Working Libraries for Radiation Transport Calculation," RSIC/DLC-113, Radiation Shielding Information Center, Oak Ridge National Laboratory (1984).

45. C. R. WEISBIN et al., "Application of FORSS Sensitivity and Methodology to Fast Reactor Benchmark Analysis," ORNL/TM-5563, Oak Ridge National Laboratory (1976); see also "FORSS: A Sensitivity and Uncertainty Analysis Code System," CCC-334, Radiation Shielding Information Center, Oak Ridge National Laboratory (1983).

46. R. L. CHILDS, D. E. BARTINE, and W. W. ENGLE, Jr., "Perturbation Theory and Sensitivity Analysis for Two-Dimensional Shielding Calculations," *Trans. Am. Nucl. Soc.*, **21**, 543 (1975).

47. R. L. CHILDS, "Generalized Perturbation Theory Using Two-Dimensional Discrete Ordinate Transport Theory," ORNL/CSD/TM-127, Oak Ridge National Laboratory (1980).

48. W. A. RHOADES and R. L. CHILDS, "An Updated Version of the DOT 4 (Version 4.3) One-and-Two-Dimensional Neutron/Photon Transport Code," ORNL-5851, Oak Ridge National Laboratory (Apr. 1982); see also CCC-429, Radiation Shielding Information Center, Oak Ridge National Laboratory (1982).

49. "DOT3.5: Two-Dimensional Discrete Ordinates Radiation Transport Code," RSIC/CCC-276, Radiation Shielding Information Center, Oak Ridge National Laboratory (1973).

50. Y. IKEDA and M. Z. YOUSSEF, "Two Dimensional Cross-Section Sensitivity and Uncertainty Analysis for Tritium Production Rate in Fusion-Oriented Integral Experiment," *Fusion Technol.*, **13**, 616 (1988).

51. M. Z. YOUSSEF et al., "Analysis of Neutronics Parameters in Phase II Experiments of the JAERI/U.S. Collaborative Program on Fusion Blanket Neutronics, Part II: Tritium Production and In-System Spectrum," *Fusion Eng. Des.*, **9**, 323 (1989).

52. K. SHIBATA et al., "Evaluation of Neutron Nuclear Data of ^{7}Li for JENDL-3," JAERI-M84-204, Japan Atomic Energy Research Institute (1984).